



## Supplementary Materials for

### **A glycerophospholipid-specific pocket in the RVFV class II fusion protein drives target membrane insertion**

P. Guardado-Calvo,\* K. Atkovska, S. A. Jeffers, N. Grau, M. Backovic, J. Pérez-Vargas, S. M. de Boer, M. A. Tortorici, G. Pehau-Arnaudet, J. Lepault, P. England, P. J. Rottier, B. J. Bosch, J. S. Hub,\* F. A. Rey,\*

\*Corresponding author. Email: pablo.guardado-calvo@pasteur.fr (P.G.-C.); jhub@gwdg.de (J.S.H.); felix.rey@pasteur.fr (F.A.R.)

Published 3 November 2017, *Science* **358**, 663 (2017)  
DOI: 10.1126/science.aal2712

#### **This PDF file includes:**

Materials and Methods  
Figs. S1 to S8  
Tables S1 to S3  
Captions for Movies S1 to S5  
References

**Other Supplementary Material for this manuscript includes the following:**  
(available at [www.sciencemag.org/content/358/6363/663/suppl/DC1](http://www.sciencemag.org/content/358/6363/663/suppl/DC1))

Movies S1 to S5

## Supplementary Materials:

### Materials and Methods

**Protein Expression and Purification.** A synthetic gene coding for the RVFV (strain 35/74) Gc ectodomain codon optimized for *Drosophila* expression, was initially inserted into a modified pMT/BiP plasmid (Invitrogen), in frame with the BiP signal sequence encoding segment upstream, and fused downstream with a segment containing the enterokinase cleavage site followed by three Strep-tag sequences separated by glycine-serine linkers (GGGS)<sub>3</sub>. This segment corresponds to residues 691-1158 in the precursor polyprotein; for consistency with the structure of the pre-fusion form (10), we also adopted the amino acid numbering corresponding to the viral polyprotein precursor from which Gc is derived (see Fig.1A). The resulting plasmid is hereafter termed pMT-Gc0. Because of solubility problems with the produced protein, we engineered this plasmid to make two other constructs: 1) construct pMT-Gc-W821H, which has the exposed Trp821 at the fusion loop mutated to histidine; and 2) construct pMT-Gc-Δ, with a deletion of the C-terminal 22 amino acids of the ectodomain (spanning aa 691-1136 in the Gc precursor), removing a region predicted to make an amphipathic α-helix immediately preceding the transmembrane segment in full-length Gc. The resulting plasmids were used to transfect *Drosophila* S2 cells together with the pCoPuro plasmid (ratio 1:20). Stable cell lines were selected and maintained in serum-free Insect-Xpress medium containing 7 μg/mL puromycin. Cultures of 1-3 L were grown in spinner flasks in Insect-Xpress medium with 1% penicillin/streptomycin antibiotics to about  $1 \times 10^7$  cells/mL, and protein expression was induced with 4 μM CdCl<sub>2</sub>. After 5 days, the S2 cells supernatant was harvested, concentrated to 40 mL, supplemented with 10 μg/mL avidin and 0.1 M Tris-HCl pH 8.0, centrifuged 30 minutes at 20,000 g and purified by streptactin affinity chromatography. Both pMT-Gc-W821H and pMT-Gc-Δ constructs resulted in secretion of large amounts of soluble and mainly trimeric protein, about 10 mg/L for Gc-W821H, and about 5-7 mg/L for Gc-Δ.

Because we subsequently found that crystallization required controlled proteolysis with trypsin, which removed the 22 C-terminal residues of Gc-W821H that were deleted in the pMT-Gc-Δ construct, all subsequent mutagenesis to make the different variants analyzed in this study were made from this construct: pMT-Gc-Δ-W821H (yielding a protein equivalent to the trypsin-treated Gc-W821H but with the purification tag sequence fused directly after position Lys1136; pMT-Gc-Δ-D961N, pMT-Gc-Δ-D961K, pMT-Gc-Δ-W821A-F826A, pMT-Gc-Δ-W821A-F826A-D961N, and pMT-Gc-Δ-W821A-F826A-D961K. These plasmids were used to transfect S2 cells as described above and produced about 5-7 mg/L of soluble protein. A first characterization by SEC and SDS-PAGE showed that wild type and mutants eluted as two peaks, corresponding to monomers and trimers, with the protein from the monomer fraction evolving into trimers with time.

For crystallization experiments, purified Gc-W821H and Gc-Δ were submitted first to deglycosylation with endo-D and then proteolysis with trypsin. Briefly, after the streptactin affinity column, the deglycosylation reaction was carried out with endoglycosidase-D (36) in 0.1 M sodium acetate pH 5.7, 0.5 M NaCl, (2% (m/m), 16 hours, 300 K) and the solution was dialyzed into 10 mM TrisHCl pH 8.0, 0.15 M NaCl and further digested with trypsin (1% (m/m),

1 hour, 300 K). The proteolytic reaction was stopped using soybean trypsin inhibitor (SBI) at a 1:1 trypsin/SBI stoichiometry, and the digest was submitted to size-exclusion chromatography using a Superdex 200 16/60 column in 10 mM TrisHCl, pH 8.0, and 150 mM NaCl. In the case of Gc- $\Delta$ , trypsin cleaves at the enterokinase site engineered between the C-terminus of the protein and the strep-tag (see above), and probably also after Ly1136, just as in the protein from the longer Gc-W821H. The proteins were then concentrated in 20 mM Bis-Tris 6.1, 150 mM NaCl using a Vivaspin centricon to 6 mg/ml and used for crystallization.

**Crystallization.** The crystallization screenings were carried out using a Mosquito robot system with 0.2  $\mu$ L of crystallization solution added to 0.2  $\mu$ L protein solution using a sitting drop vapor diffusion system. The first screens were done with commercially available solutions at 291K. Needle-shaped microcrystals of Gc-W821H grew in the presence of 35% (v/v) PEG 550 MME, 0.1 M MES pH 6.5, 10 mM ZnSO<sub>4</sub> or 25% (w/v) PEG 2000 MME, 0.1 M MES pH 6.5, 10 mM ZnSO<sub>4</sub> in about 2 weeks. Attempts to optimize growth conditions did not result in larger crystals. As the crystallization conditions were similar to those reported for monomeric and dimeric Gc (10) (18% (w/v) PEG 5000 MME, 0.1 M MES pH 6.2, 0.1M (NH<sub>4</sub>)<sub>2</sub>SO<sub>4</sub>, 1.8 mM undecyl-maltoside (UDM), and 5% glycerol), we prepared an *ad hoc* crystallization screen, which led to two new crystal forms, one of which produced high-quality diffraction. The final dataset was collected from a crystal grown in the presence of 12% (w/v) PEG 5000 MME, 0.1 M MES pH 6.2, 0.1 M (NH<sub>4</sub>)<sub>2</sub>SO<sub>4</sub>, 1.8 mM UDM, and 5% glycerol. The same approach was used to screen crystallization conditions for wild type Gc, (derived by trypsin treatment from the Gc- $\Delta$  protein). Needle-like crystals grew in 12.5-13% (w/v) PEG 5000 MME, 0.1 M Na-acetate pH 4.6, 0.1 M (NH<sub>4</sub>)<sub>2</sub>SO<sub>4</sub>, 1.8 mM UDM, and 5% glycerol, but only a few of these diffracted anisotropically and to very low resolution, and we were unable to collect useful data.

Crystals of the Gc-W821H in complex with lipid were obtained mixing the protein prepared as described above with 80 mM 1,2-dipropionyl-sn-glycero-3-phosphocholine or with 1,2-dihexanoyl-sn-glycero-3-phosphocholine (Avanti Polar lipids, hereafter referred as C<sub>3</sub>PC and C<sub>6</sub>PC). Elongated plates of the complex with C<sub>3</sub>PC grew in 14.1% (w/v) PEG 5000 MME, 0.1 M Bis-Tris pH 6.2, 0.1M (NH<sub>4</sub>)<sub>2</sub>SO<sub>4</sub>, 1.8 mM UDM, and 5% glycerol and diffracted to 2.3 Å resolution. Co-crystallization with C<sub>6</sub>PC produced crystals that diffracted poorly and were not pursued.

**Data collection and structure determination.** Optimal cryoprotection protocols for Gc-W821H crystals required supplementing the mother liquor solution with 22% (v/v) glycerol for 30-60 seconds before rapid plunging into liquid nitrogen; for crystals of the complex Gc-W821H/C<sub>3</sub>PC, the best diffraction was obtained when the crystals were cryo-cooled directly, without cryo-protection. Data were collected at beam lines Proxima1 and Proxima2 (SOLEIL Synchrotron, Paris). All data were integrated and scaled using XDS (37) and AIMLESS (38). The structure of Gc-W821H was determined by molecular replacement using the available structure of pre-fusion RVFV Gc (PDB code 4HJ1) split into three domains (domains I, II, and III) to be used separately as search models with PHASER (39). This procedure produced a clear molecular replacement solution with a translation Z-score of 13.4 and one trimer per asymmetric unit. The electron density allowed tracing the 446 N-terminal residues of the protein out of 507 in the intact trans-membrane protein (Figs. 1A and S1). We made several cycles of model

building followed by refinement using COOT (40) and PHENIX (41). The structure was validated using Molprobit (41). The crystal contains a trimer in the asymmetric unit and the final model was refined at 2.5 Å with a final  $R(R_{\text{free}}) = 19.5(23.5)\%$  and covers residues 691–1135 for chains A and B and 691–1134 for chain C. The refined model displays good geometry with only nine (0.68%) outliers in the Ramachandran plot (Val785, Ile960 in chain A, Val709, Val785, Ile960, Gly995, and Asn996 in chain B, Val785, and Ile960 in chain C). The crystal structure of the complex with C<sub>3</sub>PC was determined by molecular replacement using the model of the “apo” structure. These crystals also contain a trimer in the asymmetric unit, and the model was refined using the same procedure to 2.3 Å resolution. The refined model covers residues 691–1136 for chains A and C and 691–1134 for chain B, with internal breaks at residues 708–710 in chain A, 707–710 in chain B (A<sub>0</sub>B<sub>0</sub> loop), and 994–995 in chain C (*kl* loop). The final model was refined with a final  $R(R_{\text{free}}) = 18.3(22.4)\%$ , and six (0.46%) outliers in the Ramachandran plot (Val785 and Ile960 in the 3 chains). Complete data statistics for all structures are presented in Table S1.

**Liposome preparations.** Liposomes were freshly prepared by the freeze–thaw–and–extrusion method [10]. Briefly, lipids dissolved in chloroform were mixed, placed in glass vials and the chloroform evaporated using a SpeedVac. The dried lipids were resuspended in PBS to a final concentration of 5 mM and the preparation was submitted to ten cycles of freeze–thawing followed by extrusion through 200 nm-pore-size polycarbonate filters to generate liposomes of homogeneous size. The lipids DOPE (1,2-dioleoyl-sn-glycero-3-phosphoethanolamine), DOPC (1,2-dioleoyl-sn-glycero-3-phosphocholine), DOPS (1,2-dioleoyl-sn-glycero-3-phosphoserine), cholesterol and sphingomyelin were purchased from Avanti Polar Lipids. The ganglioside (trisialoganglioside-GT<sub>1b</sub>), and the egg yolk PC and PE was purchased from Sigma-Aldrich.

**Liposome co-floatations.** For liposome co-floatation experiments, Zika virus (ZIKV) E protein (strain H/PF/2013, KJ776791, residues 1-408), Chikungunya virus (CHKV) E1 protein (strain 91064, ABO40448.1, residues 1-412), and pseudorabies virus (suid herpesvirus 1) gB protein (strain Kaplan, AEM64049.1, residues 59-756) were produced with a tandem strep-tag in the Drosophila Expression System (Invitrogen) as described above. Once the protein was purified, 1 mM liposomes were incubated with 1 μM protein in 0.1 M MES pH 5.5, 0.15 M NaCl at 30°C overnight, in the final volume of 130 μl. Liposomes and liposome-protein complexes were separated from unbound protein by ultracentrifugation of the reaction mixture in 5 mL Optiprep™ (Axis-Shield PoC AS) density gradients for 1 hour at 40,000 × *g* (SW55Ti Beckman Coulter rotor). The liposome-protein mixture was adjusted to 34% Optiprep concentration in a volume of 300 μl, and loaded onto the bottom of the tube that contained 4.5 ml of 20% Optiprep in 0.1 M MES pH 5.5, 0.15 M NaCl, overlaid with 200 μl of the buffer. The top fraction and bottom fraction, containing 400 μl and 600 μl of the gradient, respectively, were used for SDS–PAGE gel analysis and immunoblotting against strep-tag. For the liposome co-floatation experiment of FigS8B, panel ii, 2 mM liposomes were incubated with 1 μM protein in 0.1 M MES pH 5.5, 0.15 M NaCl at 25°C overnight, and liposomes and liposome–protein complexes were separated from unbound protein by ultracentrifugation in a sucrose (from 60% to 5%) gradient for 13 hours at 34,000 rpm in a SW 41 rotor. Four fractions, from the top to the bottom of 2 mL (T1), 1 mL (T2), 3.5 mL (M) and 3.5 mL (B) were collected and used for SDS–PAGE gel analysis and immunoblotting against strep-tag.

**Electron microscopy.** The micrographs shown in Figure 1 correspond to proteoliposomes prepared as follows: 200 ng of Gc were added to 10  $\mu$ l of a liposome solution in PBS composed of egg yolk PC/egg yolk PE/ganglioside/cholesterol in ratios (1/1/1/1.5) (pH 7.4). After 1 minute incubation at room temperature, the sample was spotted to carbon coated glow discharged grids, contrasted with 2% (w/v) uranyl acetate and screened on a Philips CM2 microscope operating at an accelerating voltage of 80 kV. For the micrographs shown in Fig. S4, 200 ng of Gc were incubated with 10  $\mu$ l of a solution of liposomes composed of DOPC/DOPE/sphingomyelin/cholesterol (1/1/1/3), negatively stained with phosphotungstic acid and screened with a Tecnai G2 Spirit Biotwin microscope 5 (FEI, USA) at an accelerating voltage of 120 kV.

**Surface Plasmon Resonance (SPR) experiments.** The Gc variants used in the SPR and BLI liposome binding experiments were purified first by streptactin affinity followed by size exclusion chromatography, and only the trimeric fraction was used. The SPR experiments were performed at 25°C using a Proteon XPR36 (BioRad) instrument equilibrated in PBS buffer. The liposomes were captured on GLC chips that had been previously functionalized with undecylamine molecules by amine coupling. The liposome immobilization procedure was as follows: after washing the surface of the chip using sequential injections of 20 mM CHAPS and a mixture of 40% (v/v) isopropanol and 30 mM NaOH, liposomes with the following compositions were injected at 30  $\mu$ L/min during 300 seconds: DOPC, DOPC/cholesterol (1/1), DOPC/DOPS (7/1), DOPC:DOPS (3/1), DOPC/DOPS/cholesterol (3/1/4), and DOPC/DOPS/cholesterol (1/1/2). The lipid concentrations were adjusted to reach comparable densities (7000-8000 RU) for all liposomes. The flow cells were saturated by injecting a solution of BSA (0.2 mg/mL) diluted in PBS (180 sec, 30  $\mu$ L/min) to minimize non-specific adsorption phenomena due to the presence of remaining free undecylamine groups. The microfluidic cartridge of the instrument was then rotated and six different proteins were injected at 50 nM (120 sec, 50  $\mu$ L/min) over the captured liposomes: wild type Gc, and the *ij* loop mutants Gc-D961N and Gc-D961K, together with their respective fusion loop mutants used as negative controls: Gc-W821A-F826A, Gc-W821A-F826A-D961N, Gc-W821A-F826A-D961K. The single mutant Gc-W821H gave similarly negative signals. Dissociation of the complexes formed was monitored for 300 seconds. All the experiments were done in duplicate. The final SPR profiles were referenced by subtracting the signal measured on the control surface (with cholesterol-free liposomes).

**BLI assays.** In order to confirm the SPR data and minimize potential experimental artifacts, we performed reverse assays i.e. instead of immobilizing liposomes, we immobilized the proteins (Gc-wt, Gc-W821H, Gc-D961N, and Gc-D961K) on Octet BLI sensor surfaces (ForteBio). Streptavidin (SA) sensors were incubated in an OctetRed 384 system (ForteBio) with mildly biotinylated protein solutions (200 nM) until a signal shift of 2.1–2.3 nm was obtained. The functionalized sensors were then washed for 120 s in PBS-BSA (0.2 mg/mL) before dipping for 600 s into solutions of liposomes diluted in PBS-BSA to a final concentration of 100  $\mu$ M. Dissociation of the liposome/protein complexes was then monitored in PBS-BSA for 300 s. All the experiments were performed in duplicate on two different sensors to account for potential experimental artifacts due to inter-sensor variability. In all cases, potential non-specific

interactions were monitored using a sensor coated with the fusion loop mutant Gc-W821H as a negative control. The curves were processed using BiaEvaluation software (Biacore).

**Sequence alignment of flavivirus and alphaviruses representatives.** For the alignment shown in the Figure 4 we used 10 flavivirus and 13 alphavirus representatives with the following accession codes: **Flaviviruses.** DENV1: Dengue virus serotype 1 (ACN42679.1); DENV2: Dengue virus serotype 2 (NP\_056776.2); DENV3: Dengue virus serotype 3 (ACA58335.1); DENV4 (Dengue virus serotype 4 (Q2YHF0.1); TBEV: Tick-borne encephalitis virus (NP\_043135.1); POWV: Powassan virus (NP\_620099.1); JEV: Japanese encephalitis virus (ABQ52691.1); WNV: West Nile virus (YP\_001527877.1); YFV: Yellow Fever virus (Q6DV88.1); ZKV: Zika virus (AOO19564.1). **Alphaviruses.** CHKV: Chikungunya virus (CAJ90470.1), ONNV: O'nyong nyong virus (AAC97205.1); RRV: Ross River virus (AAA47404.1); SAGV: Sagiyama virus (AAO33337.1), SFV: Semliki Forest virus (CAA27742.1); MAYAV: Mayaro virus (AAO33335.1); MIDDV: (Middleburg virus (AA033343.1); BFV: Barmah Forest virus (AA033347.1), AURAV: Aura virus (AAD13623.1); SINV: Sindbis virus (AAA96976.1); WEEV: Western Equine Encephalitis virus (AAA42999.1); VEEV Venezuelan Equine Encephalitis virus (ABB45866.1).

**Molecular dynamics (MD) simulations.** Atomistic MD simulations were performed with Gromacs 4.6 (42). The protein and lipids were described by the Amber-99SB\*-ILDN and Slipids force fields, and water was described using the TIP3P model (43-46). All systems were neutralized by counter ions. The temperature was kept at 310 K during production simulations, and at higher temperatures during equilibration (see below), using velocity rescaling ( $\tau = 2.5$  ps) (47). The pressure was controlled at 1 bar using the semiisotropic Berendsen ( $\tau = 2$  ps) and Parrinello-Rahman barostats ( $\tau = 5$  ps) during equilibration and production runs, respectively (48, 49), whereby the scaling in the *xy*-plane was independent from the scaling in the *z*-direction. Electrostatic interactions were calculated with the particle-mesh Ewald method with a real space cut-off at 1 nm (50, 51). Dispersion interactions and short-range repulsion were described together by a Lennard-Jones potential with a cutoff of 1.4 nm (unless stated otherwise). The SETTLE algorithm was used to constrain the bond lengths and angles of the water molecules, while all other bonds were constrained using LINCS (52, 53). An integration step of 2 fs was used. In total, the simulation systems contained ~120,000–166,000 atoms, including protein, 177–386 lipids, ~25,000–35,000 water molecules, and 36 sodium ions.

*MD simulations setup.* In total, six MD simulation systems were set up (Table S2). We used the structure of the Gc-W821H ectodomain in complex with C<sub>3</sub>PC, which has higher resolution (last column in Table S1), in which we in silico mutated back *His821* to the wild-type Trp and removed the C<sub>3</sub>PC molecule with Pymol (54). The sugar residues (linked to *Asn794*) and the C<sub>3</sub>PC lipids were removed. Pre-equilibrated membrane patches containing 128 lipids (DOPC and 0%-50% cholesterol, in steps of 10%) and 5120 water molecules were downloaded from <http://mmkluster.fos.su.se/slipids/Downloads.html>. These were used to create six larger systems in a box shaped as a hexagonal prism, with membrane areas between 58 and 78 nm<sup>2</sup> (the actual size depended on the total number of lipids in the box). The hexagonal membrane patches contained the following number of lipids: 177 DOPC; 182 DOPC + 21 cholesterols; 175 DOPC + 46 cholesterols; 169 DOPC + 75 cholesterols; 172 DOPC + 119 cholesterols; and 191 DOPC + 195 cholesterols, resulting with approximately 0%, 10%, 20%, 30%, 40%, and 50% cholesterol,

respectively, with a maximum absolute deviation of 0.9%. These patches were equilibrated until the box dimensions and potential energies converged (10–40 ns). Next, the protein trimer was added to the system with its axis centered and positioned perpendicular to the membrane, at a distance from the membrane such that the residues at the very tip of the trimer were as close as possible to the lipid heads without causing clashes. Water molecules overlapping with the protein were removed. The box was extended in the  $z$ -direction (perpendicular to the membrane) so as to fit the trimer and the bilayer (total box height:  $\sim 20$  nm), and was fully hydrated. A typical simulation box is shown in Fig. S6A.

*Equilibration procedure.* In order to account for the slow convergence of the lipid-protein interactions, we equilibrated the protein/membrane systems using a combination of center-of-mass pulling, center-of-mass restraints, and equilibration at increased temperature, as outlined in the diagram of Fig. S6A. The procedure consisted of the following steps:

- 1.) First, in order to force the protein into the membrane, we pulled the membrane towards the protein by continuously reducing the distance between the respective centers of mass. This was achieved by a harmonic potential with force constant of 1000 or 2000  $\text{kJ mol}^{-1} \text{nm}^{-2}$  and pull velocity of 1 or  $2 \times 10^{-4} \text{nm ps}^{-1}$ , depending on the case (see Table S2). The pulling force was applied for 17–35 ns, during which the distance between the protein and the membrane was reduced by  $\sim 1.4$  nm on average.

- 2.) Next, to accelerate the lateral equilibration of the lipids, as well as the recovery of the bilayer from the distortions caused by the pulling in the previous step, the system was simulated for a minimum of 70 ns at higher temperature (403 K for the 50% cholesterol system, and 373 K for all other systems), while keeping the protein-membrane distance restrained with a harmonic potential with force constant of  $4000 \text{kJ mol}^{-1} \text{nm}^{-2}$ . Henceforth, the temperature was kept at 310 K.

3. In a subsequent simulation of 5 ns, the protein-membrane distance restraint was released. All heavy atoms in the protein were kept restrained in steps 1–3.

*The MD production runs.* The position restraints acting on the protein were released, with exception of the  $C_\alpha$  atoms from the upper third of the protein, which were always held restrained in the  $xy$ -plane (membrane plane) to prevent the trimer axis of the protein to tilt with respect to the membrane. No restraints were applied in the  $z$ -direction (normal to the membrane and along the 3-fold symmetry axis), hence allowing the simulation to equilibrate the penetration depth of the protein into the membrane. Initially, three or four production runs of 450–600 ns each were performed for each cholesterol concentration (Table S2). We found significant fluctuations in the analyzed quantities during the first several hundred nanoseconds, therefore, we discarded the first 200–400 ns of each simulation run for further equilibration. The analyses performed considering the last 200 ns of each simulation already revealed trends in the calculated quantities (defined below), depending on cholesterol content. To validate the robustness of the observed trends over longer time scales, we continued each simulation for additional 500 ns, using a shorter cutoff of 1.2 nm for the Lennard-Jones interactions, in order to maintain computational feasibility. After discarding the first 20 ns for equilibration with the new cutoff, we found the same trends persist. The data shown in Figures 3A, 3E and S7A were obtained by combining the last 200 ns of the initial simulations and the last 480 ns of the continued simulations, resulting in total with 2–2.7  $\mu\text{s}$  per cholesterol concentration used for the analyses. The total simulation time for all cholesterol concentrations and including equilibration adds up to  $\sim 22 \mu\text{s}$ .

*Parameters quantified at the end of the production runs.* The penetration depth  $d_{\text{protein-lipid}}$  of the protein into the membrane (Fig. 3E, upper panel) was quantified as the distance along the  $z$ -direction between the centers of mass of the protein and of the phosphate atoms of the lipids in the leaflet in contact with the protein. The data are shown relative to  $d_{\text{protein-lipid}}$  at 0% cholesterol (59.99 Å).

The potential energy  $V_{\text{protein-lipid}}$  between the protein and the membrane (Fig. 3E, second panel from the top) was calculated as the sum of the short-range Coulomb and Lennard–Jones energies between the protein and the lipid molecules.

The number of hydrogen bonds (Fig. 3E, third panel from the top) between the protein and the lipids was estimated with the `g_hbond` tool implemented in Gromacs (11), using the default settings: all NH and OH groups were considered donors, and all O and N atoms were considered acceptors, the donor–acceptor distance cutoff was 3.5 Å, and the hydrogen-donor–acceptor angle cutoff was 30°.

The cholesterol enrichment at the membrane/protein contact area (Fig. 3E, bottom panel) was computed as follows. The membrane was decomposed into (i) a circular area  $A_{\text{in}}$  of radius 1.9 nm centered at the protein's three-fold symmetry axis, and (ii) the remaining membrane area,  $A_{\text{out}}$ . Hence,  $A_{\text{in}} + A_{\text{out}}$  was the cross–section area of the simulation box. The enrichment was defined as  $\phi = \rho_{\text{in}}/\rho_{\text{out}}$ , where  $\rho_{\text{in}}$  and  $\rho_{\text{out}}$  denote the cholesterol number density within  $A_{\text{in}}$  and  $A_{\text{out}}$ , respectively, as averaged over 3 (or 4)  $\times$  680 ns of equilibrium simulation time. Only cholesterol molecules in the membrane leaflet in contact with the protein were used to compute  $\rho_{\text{in}}/\rho_{\text{out}}$ .

For all calculated quantities, average values (full black circles in Fig. 3E) are shown with standard errors computed by block averaging (55). The average values from individual simulation runs exhibit significant variation (open triangles, Fig. 3E), demonstrating that an average over multiple long simulation replicas, as used here, is required to achieve reasonably converged values for  $d_{\text{protein-lipid}}$ ,  $V_{\text{protein-lipid}}$ , the number of hydrogen bonds, and for the cholesterol enrichment,  $\phi$ .

*Cholesterol density distribution on the outer leaflet.* The cholesterol two-dimensional (2D) densities  $\rho_{2D}$  in the leaflet in contact with the protein (Figs. 3A and S7A, top row) were computed as an average over 3 (or 4)  $\times$  680 ns of equilibrium simulation time (Table S2) of the corresponding cholesterol concentration considering the center of mass of each cholesterol molecule. In order to visualize the cholesterol enrichment also at lower cholesterol concentrations, we plotted the relative 2D densities  $\rho_{2D}/\langle\rho_{2D}\rangle$  (Fig. S7A, bottom row), where  $\langle\rho_{2D}\rangle$  denotes the 2D density averaged over the entire membrane leaflet. Hence,  $\langle\rho_{2D}\rangle$  was given by the number of cholesterol molecules in the upper leaflet divided by the total membrane area.

*Free energy calculations.* For calculation of the difference in the free energy of binding of the wild-type protein and three mutants (W821H, W821A, and W821A/F826A) to the membrane, the thermodynamic cycle shown in figure S6B was constructed. The discrete thermodynamic integration method was used to perform the alchemical perturbation in the two branches (membrane-bound protein, yielding  $\Delta G_{\text{m}}$ , and unbound protein in solution, yielding  $\Delta G_{\text{s}}$ ). The difference between the free energies of binding of the wild type and mutant protein was then calculated as:  $\Delta\Delta G_{\text{binding}} = \Delta G_{\text{binding}}(\text{mutant}) - \Delta G_{\text{binding}}(\text{WT}) = \Delta G_{\text{m}} - \Delta G_{\text{s}}$  (Fig. S6B). The starting structure for the “membrane bound” branch was obtained from the final snapshot of

one of the production runs at 30% cholesterol. For the “in solution” branch, the protein was equilibrated for 20 ns in water (the same crystal structure with the same modifications as for all other simulations was used). The hybrid structures and topologies were generated using the pmx topology generator (58). For both branches, the energy of the system was minimized, after which a quick, continuous perturbation from  $\lambda = 0$  (wild type protein) to  $\lambda = 1$  (mutant) was performed in 1 ns. This trajectory was used to spawn the starting structures for the discrete TI steps. The Coulomb and LJ interactions were perturbed simultaneously employing soft core potential for all non-bonded interactions (59). For the W821H transformation, 36 TI steps with duration of 10 ns were simulated in each branch. For the double mutant, the mutations were done in two consecutive steps. First, the wild-type protein was transformed into the W821A mutant (in 36 TI steps of 10 ns in each branch). Then, the final snapshots from the TI steps at  $\lambda = 1$  were used as starting structures to transform the W821A mutant into the W821A/F826A double mutant, which was also performed in 36 TI steps of 10 ns in each branch. The resulting  $\Delta\Delta G_{\text{binding}}$  from the first step represents the difference in the binding free energy between the wild-type protein and the W821A mutant, whereas the sum of the resulting  $\Delta\Delta G_{\text{binding}}$  values from both steps represents the difference in the binding free energy between the wild type protein and the double mutant. For all transformations,  $\Delta G_s$  and  $\Delta G_m$  (Table S3) were calculated using the `g_analyze` module implemented in Gromacs (11), by averaging  $\partial H/\partial\lambda$  from each simulation (discarding the first nanosecond for equilibration, and estimating the error using block averaging), and subsequent integration over  $\lambda$  using the trapezium rule.

**Additional Author notes:** FAR and PGC designed the experiments. PGC, SAJ, SMB, JPV, PJR, BJB cloned the constructs expressing the recombinant proteins. PGC produced and purified the recombinant proteins. PGC grew the crystals, collected synchrotron data, processed the data and built the atomic models. FAR and PGC analyze the atomic models. PGC and PE performed the SPR and BLI experiments. MAT prepared the liposomes for the SPR, BLI and electron microscopy experiments. PGC, GPA and JL performed the electron microscopy experiments. NG and MB performed the liposome flotation experiments. KA and JSH designed the MD simulations. KA ran and analyzed simulations. PGC, FAR, KA, and JSH wrote the paper.

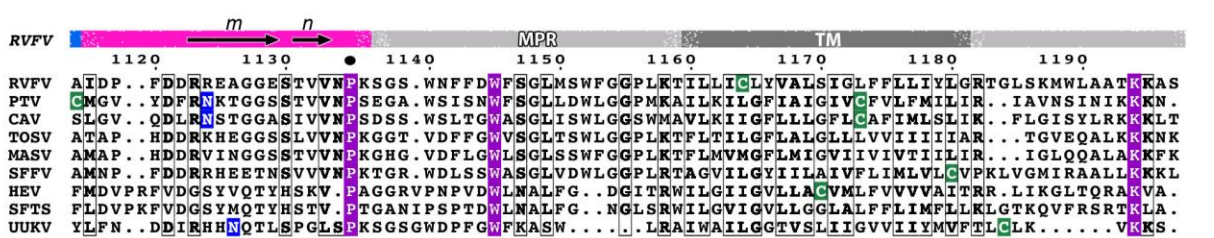
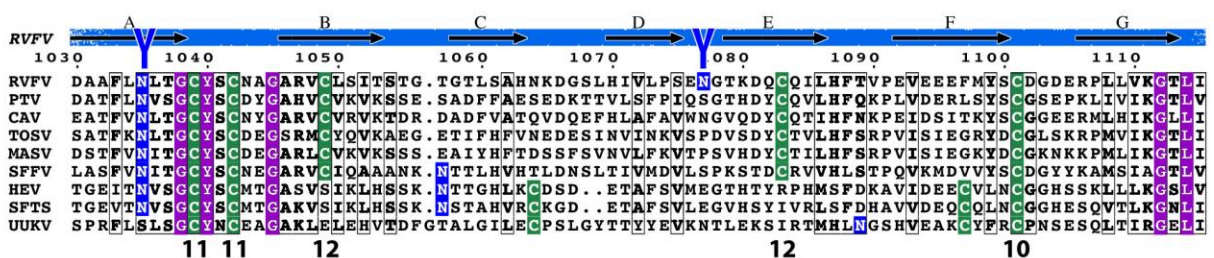
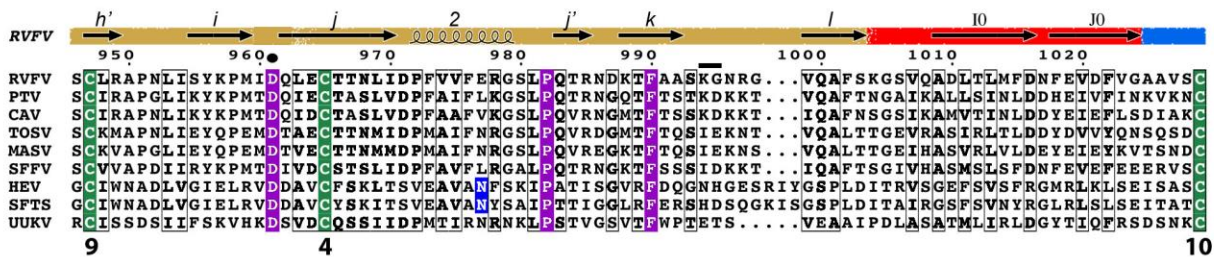
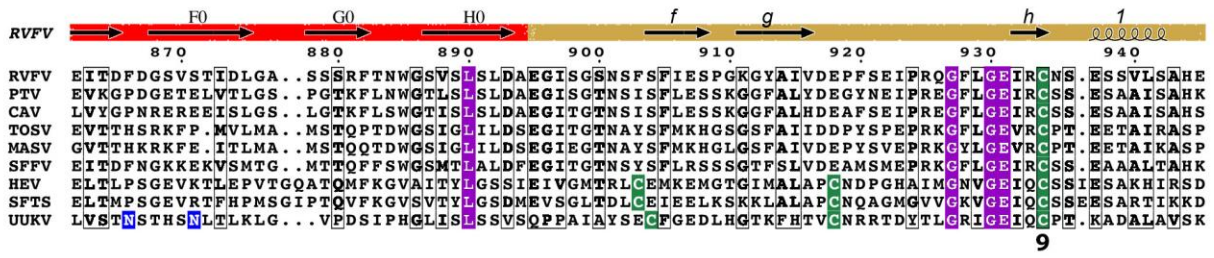
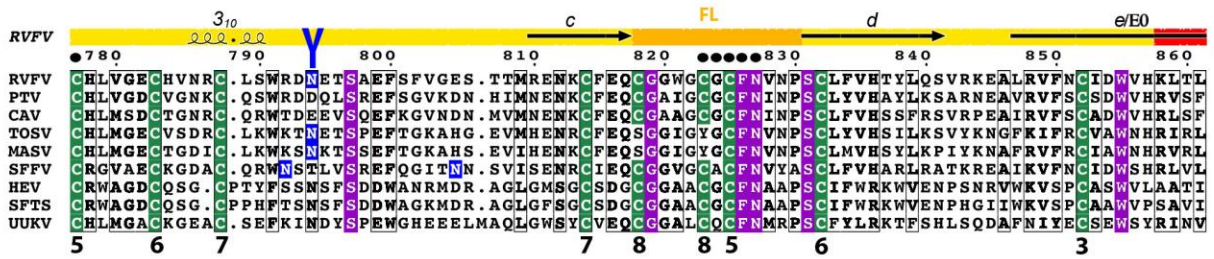
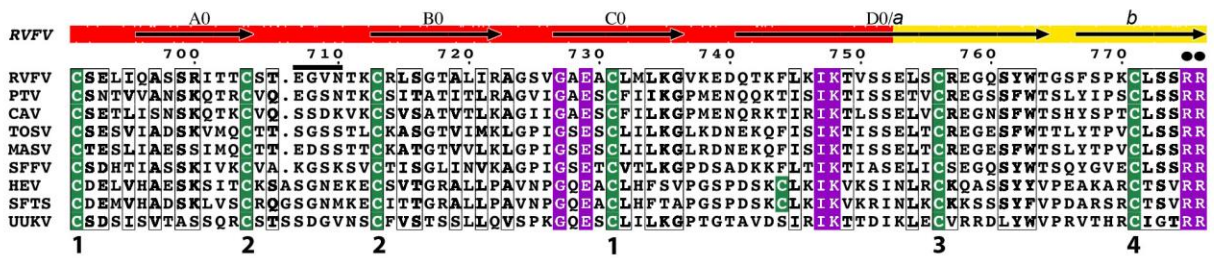
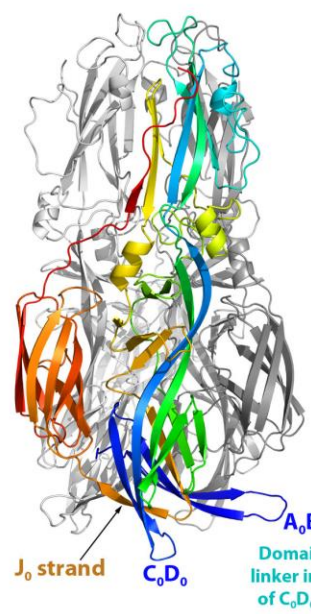
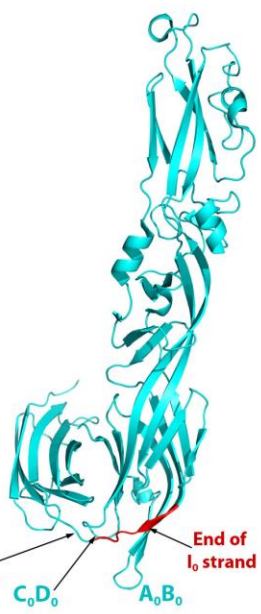


**Fig S1. Gc Amino acid sequence alignment of representative members of the *Phlebovirus* genus.** The top five viruses are insect-borne (mosquitoes or sand flies) and the last three tick-borne phleboviruses. Conserved positions are in a magenta background. All cysteines are shown on a green background and asparagine residues within *N*-linked glycosylation motifs are shown in a blue background. Glycans with visible electron density in the RVFV Gc structure are indicated with a blue “Y” above the sequences. Disulfide bonds in RVFV are numbered in black below the sequences. Solid black circles above the alignment mark residues in the C<sub>3</sub>PC binding pocket. The secondary structure elements are displayed above the sequences, on a bar colored-coded according to the tertiary structure, as in Figure 1 (domain I: red, domain II: yellow and beige with the fusion loop in orange, domain III: blue and stem: magenta; segments in grey are not resolved in the crystals. MPR: Membrane proximal region; TM: trans-membrane segment; PTV: Puntatoro virus (AAA47110.1); CAV: Candiru virus (AEA30045.1); TOSV: Toscana virus (ABS85172.1); MASV: Massilia virus (ACI24011.1); SFFV: Sandfly fever virus (AAA75043.1); HEV: (Heartland virus, AFP33393.1); SFTSV: Severe Fever with Thrombocytopenia Syndrome virus (ADZ04471.1); UUKV: Uukuniemi virus (38371706).

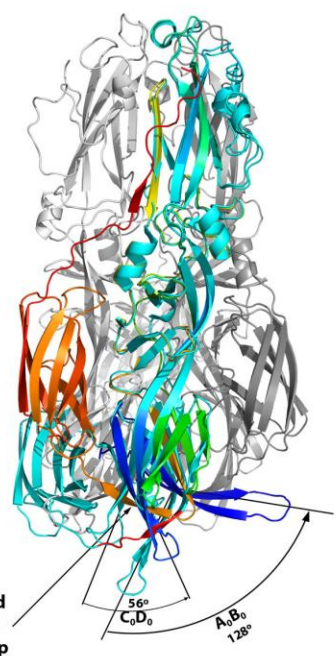
**A Post-fusion form**  
 N  C



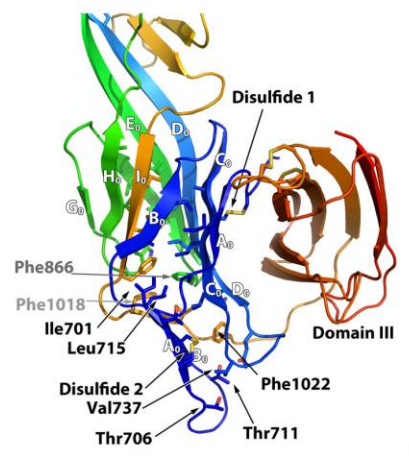
**B Pre-fusion form**



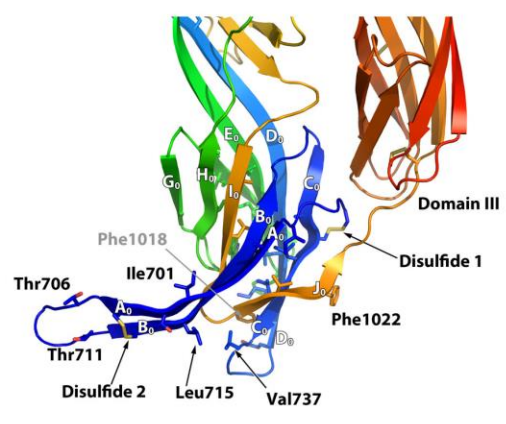
**C Superposition**



**D Pre-fusion form**



**E Post-fusion form**



**F Post-fusion trimer**

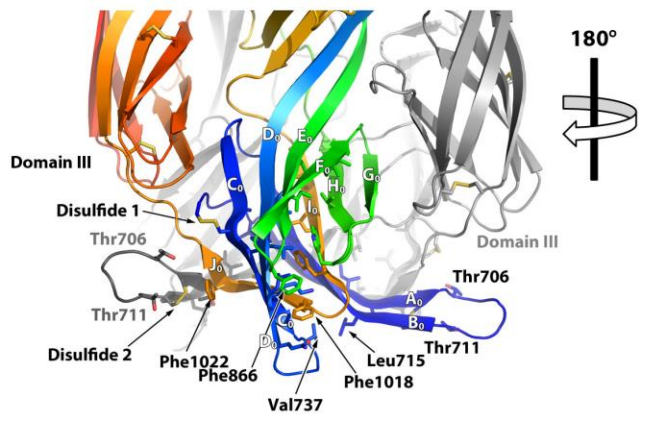


**Fig S2. Structural reorganization of Gc to reach the post-fusion conformation** A) Crystal structure of the postfusion trimer of RVFV with the subunit in the foreground rainbow-colored from N- to C-terminus as indicated in the bar on top, and the other two in gray. B) Crystal structure of RVFV Gc in prefusion conformation (PDB 4HJ1) colored cyan with the residues corresponding to the postfusion J<sub>0</sub> strand in red. C) Superposition of the prefusion protomer on the foreground subunit (color coded as in A and B) of the post-fusion trimer. The rotation angles of the A<sub>0</sub>B<sub>0</sub> and C<sub>0</sub>D<sub>0</sub> loops are indicated. See Movie S2 for a morph of the transition. D) Close-up view of domain I in the pre-fusion form rainbow-colored as above, with the residues stabilizing the core of the domain I β-barrel represented as sticks and labeled. E) Corresponding view of the postfusion domain I in the same orientation as in D, with the same residues labeled and represented as sticks. F) Close-up view of domain I in the context of the postfusion trimer rotated 180° from E) to show inter-protomer interactions. See Movie S3, which highlights the relocation of the side chains of *Phe1018* and *Phe1022* from the domain I core in the pre-fusion form to the inter-subunit packing in the post-fusion trimer.

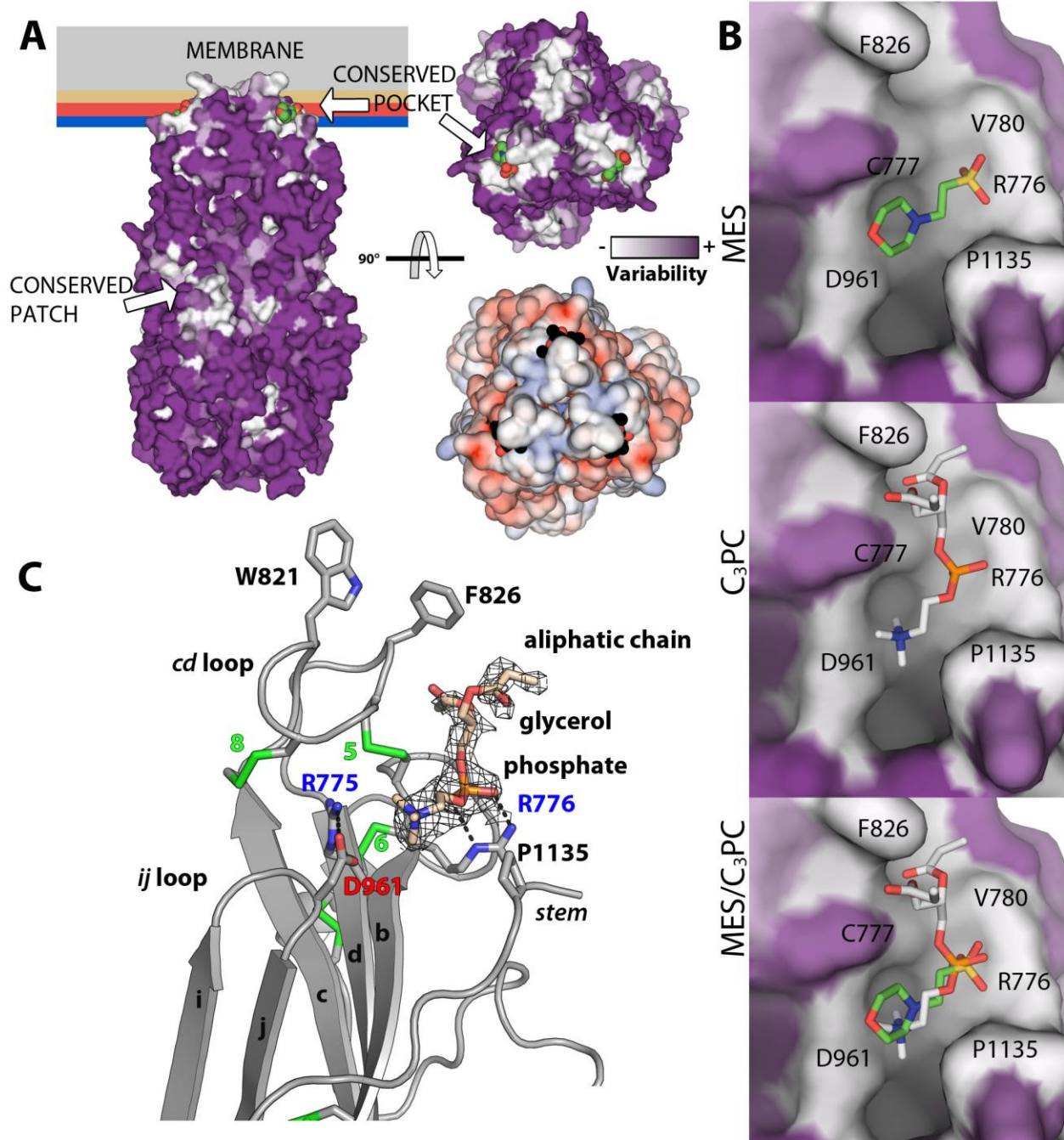


**Fig S3. Surface properties and MES–C<sub>3</sub>PC binding.** A) Surface representation of the Gc post-fusion trimer in a side (left panel) and top view from the membrane (right panels). Left and top right panels are colored according the degree of sequence conservation across the *Phlebovirus* genus from white (conserved) to purple (variable) as shown in the color key bar. The MES molecule, present in two protomers of the trimer only, is represented as spheres with carbon atoms colored green and sulfur, oxygen and nitrogen yellow, red and blue, respectively. Note that MES binds in a strictly conserved pocket. The second row in panel A (to the right) shows the surface of Gc from the structure in complex with C<sub>3</sub>PC colored according to electrostatic

potential from -5 kT/e (red) to +5 kT/e (blue), white being neutral. C<sub>3</sub>PC (present in all three protomers in these crystals) is shown as spheres colored black and red for carbon and oxygen atoms, respectively. B) Close-up views of the lipid binding pocket colored by conservation with MES (upper panel), C<sub>3</sub>PC (central panel), and both superposed (lower panel). MES is colored as in A, but C<sub>3</sub>PC is shown here with carbon atoms white. The conserved residues involved in C<sub>3</sub>PC binding are labeled. C) Cartoon representation of the C<sub>3</sub>PC binding groove with the residues implicated in the interaction shown as sticks and labeled. The lipid is also shown as sticks with the carbons colored wheat and a 2Fo-Fc omit map around the lipid contoured at 0.7  $\sigma$  is shown as mesh (see Movie S4). To calculate the omit map the atoms of the lipid were removed, B-factors reset to 30  $\text{\AA}^2$  and one round of cartesian simulated annealing was done to remove model bias.

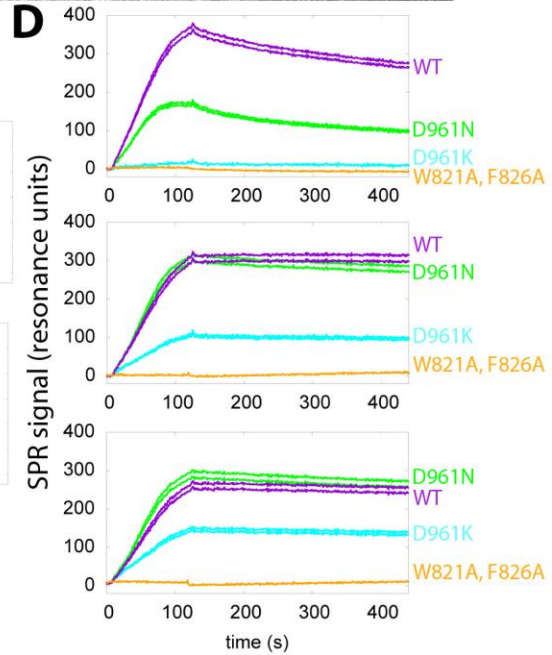
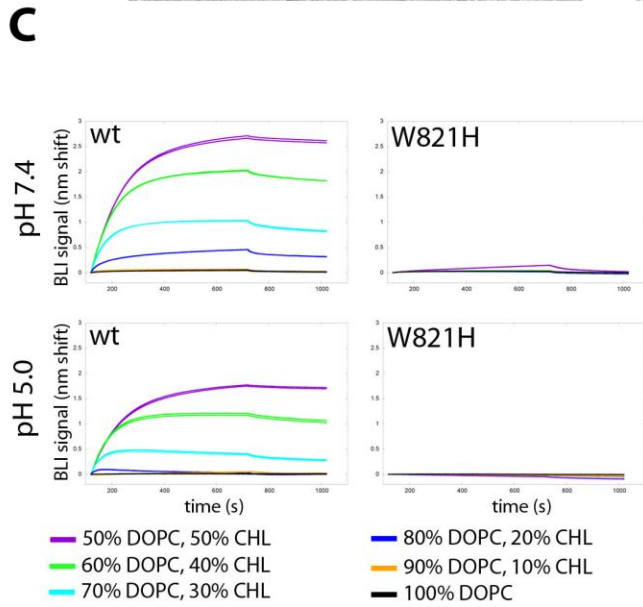
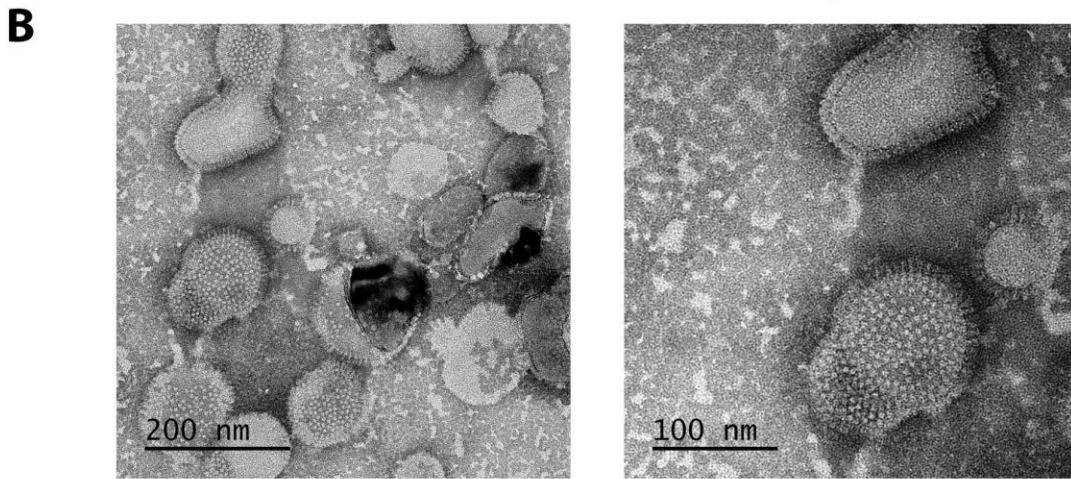
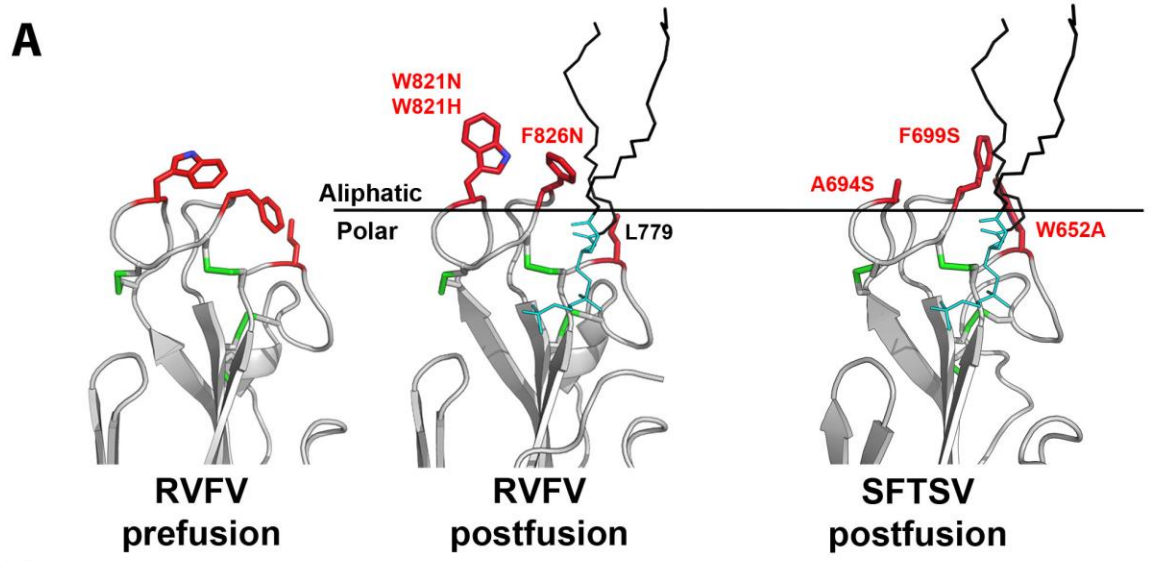


**Fig S4. Characterization of the interaction of Gc with liposomes.** A) Cartoon representation of the tip of domain II from RVFV Gc in the prefusion conformation (left panel, PDB code 4HJ1), in postfusion conformation (middle panel, PDB code 6EGU) and Gc from SFTSV in postfusion conformation (right panel, PDB code 5G47). A DOPC lipid was superposed to the C<sub>3</sub>PC lipid of the crystal structure, and is shown in cyan (head group) and black (aliphatic chains). The lipid fits equally well in SFTSV Gc (right panel). The main chain conformation is virtually identical with C $\alpha$  RMSD values of 0.36 (prefusion RVFV /postfusion RVFV) and 1.09 (postfusion RVFV/ postfusion SFTSV). The main differences in the RVFV structures are in the rotamers adopted by *Trp821* and *Phe826*, which are involved in dimer contacts in the prefusion homodimer. The salt bridge between *Arg775* and *Asp961*, which binds the trimethylamine of choline, and the conformation of *Arg776*, which interacts with the phosphate, is conserved in the three structures. The residues inserting into the aliphatic moiety of the membrane are indicated in sticks with carbon atoms in red and the mutations that render Gc non-functional are labeled in red (18, 26). B) Electron micrographs of negatively stained samples of Gc inserted into liposomes made of DOPC/DOPE/sphingomyelin/cholesterol (1/1/1/3) C) Requirement for cholesterol: BLI sensorgrams showing the interaction with liposomes composed of DOPC and cholesterol at different ratios at pH 7.4 (top panels) and pH 5 (bottom panels) by wild type Gc (left panels) and the control W821H mutant (right panels). The Gc ectodomain spontaneously trimerizes and the trimers bind to the liposomes both at neutral and acidic pH D) SPR sensorgrams showing the interaction of Gc WT, D961N, D961K, and the double mutant W821A-F826A with liposomes containing 50% cholesterol with 50% DOPC (upper panel), with 37.5% DOPC and 12.5% DOPS (middle panel), and with 25% DOPC and 25% DOPS (lower panel).

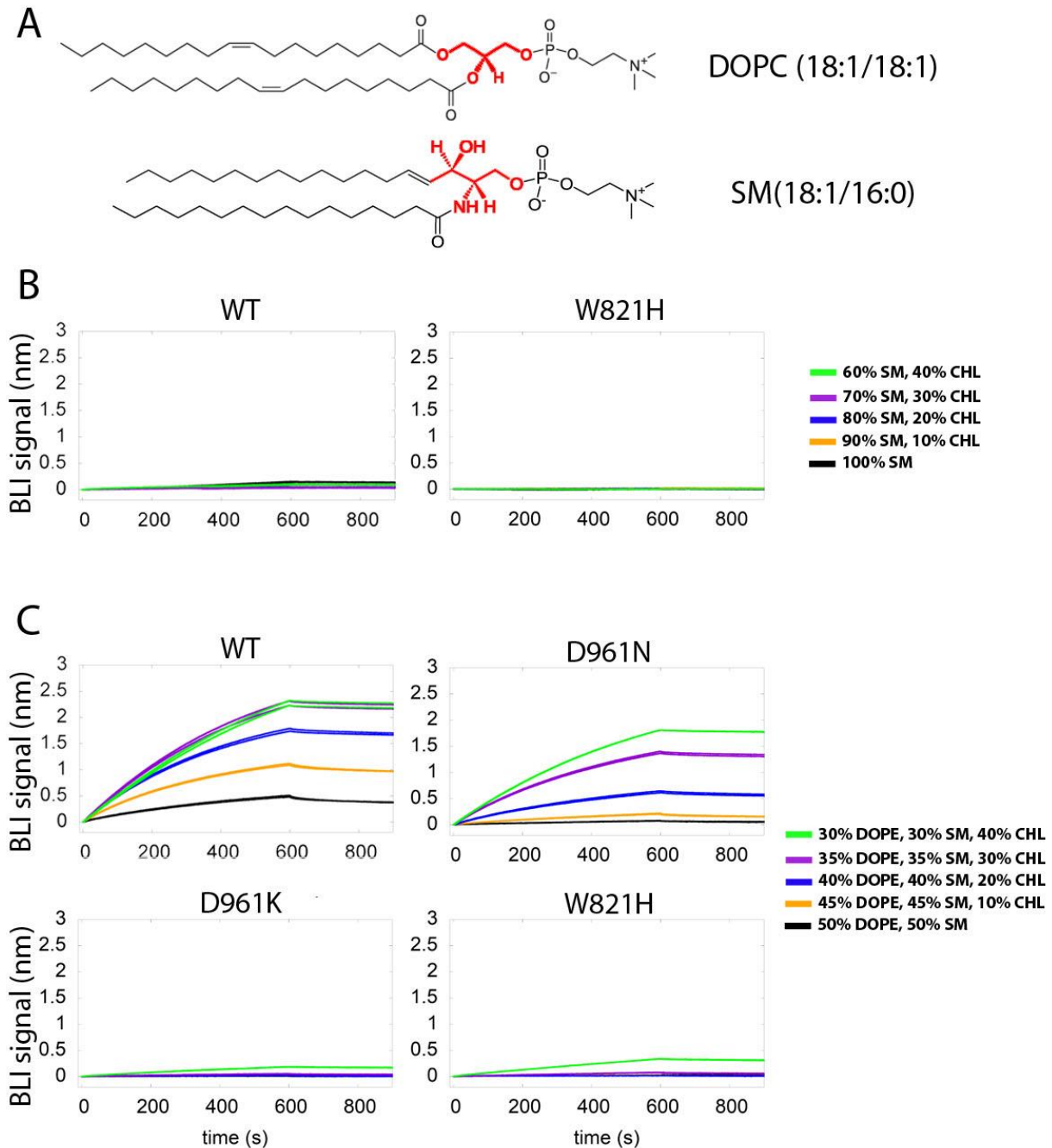


**Figure S5.** A) Comparison of the chemical structures of DOPC and SM with the differences highlighted in red. B) BLI sensorgrams showing the interaction of Gc-WT and Gc-W821H with liposomes composed of SM and cholesterol at different ratios, as indicated, showing that addition of cholesterol does not rescue binding. C) BLI sensorgrams showing the interaction of Gc-WT, Gc-D961N, Gc-D961K, and Gc-W821H with liposomes composed of SM:DOPE:cholesterol at different ratios, as indicated, showing that PE rescues binding for the wild type and D961N mutant.

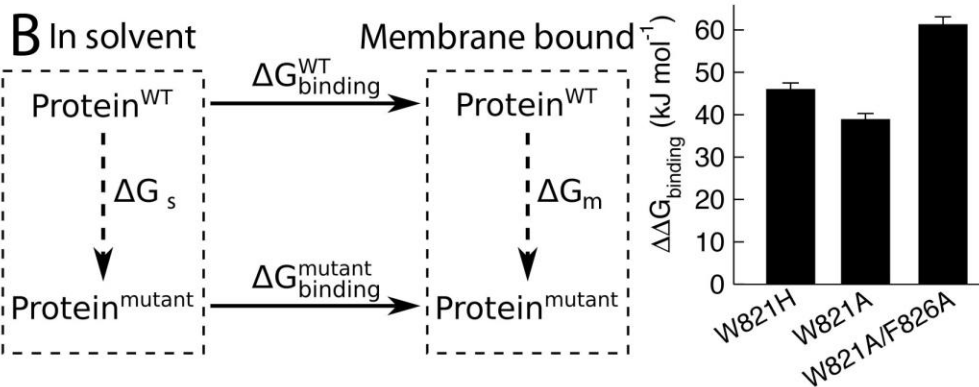
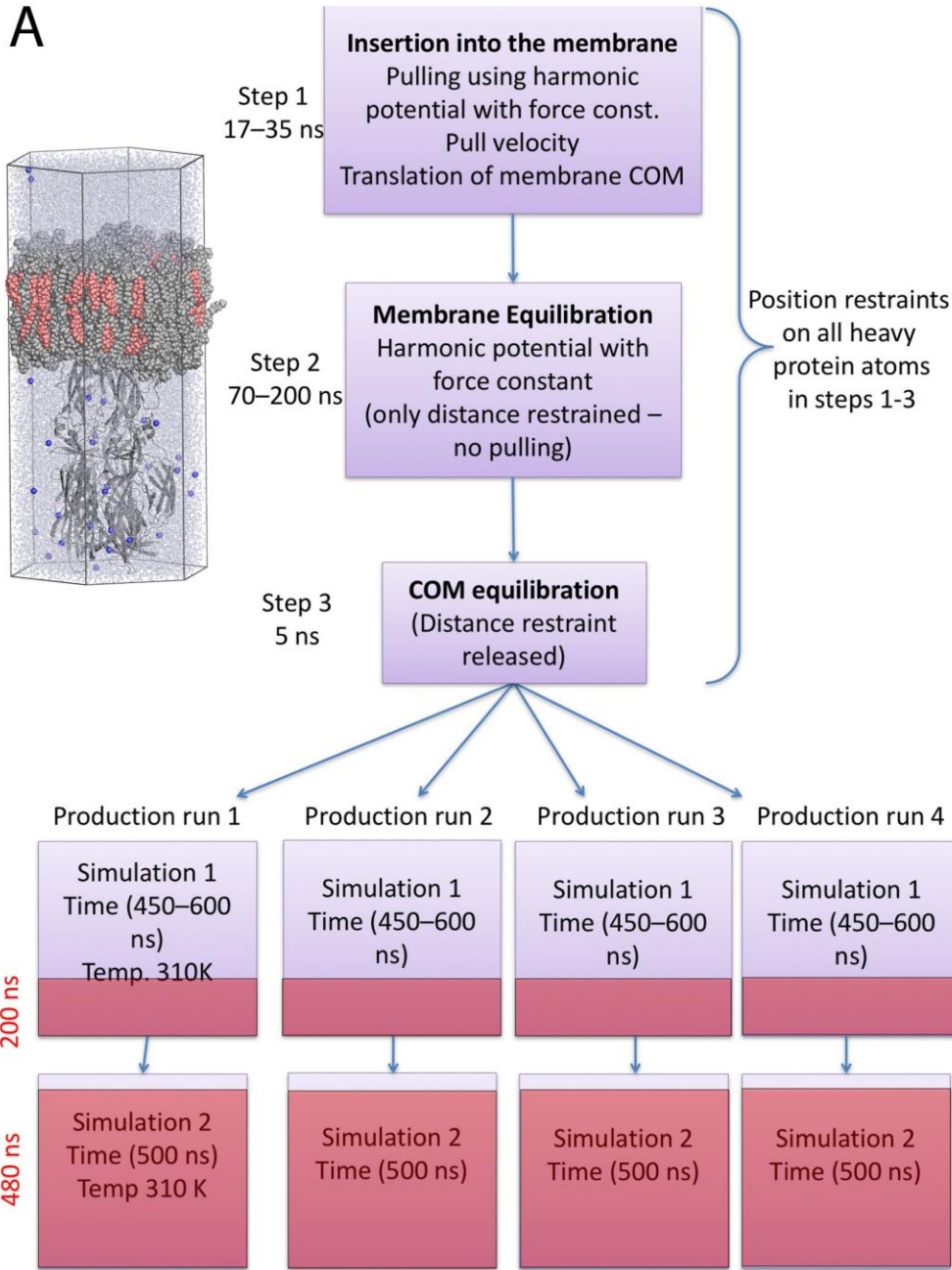


**Fig S6. MD simulation flow scheme.** A) Left panel: a typical box used for the MD simulations, in which the protein is shown as a gray ribbon and the lipids as spheres, with PC in grey and cholesterol in red. Water molecules are represented as small blue dots throughout the box, and  $\text{Na}^+$  counter ions as blue spheres. Right panel: diagram outlining the steps followed during the MD simulations. In the first three steps the positions of the protein atoms were restrained, to be then released as explained in the text. The ensuing simulations were done in three or four independent production runs (as indicated in Table S2), and the last 680 ns of each run (highlighted in pink in the respective boxes) were used in the analyses presented in Figs. 3 and S7. B) Left panel: Thermodynamic cycle for calculation of  $\Delta\Delta G_{\text{binding}}$ . The dashed arrows denote the simulated branches, where  $\Delta G_s$  and  $\Delta G_m$  correspond to the free energies of the wild type to mutant transformation in the unbound and bound protein, respectively. The difference between the free energies of binding of the wild type and mutant protein is calculated as:  $\Delta\Delta G_{\text{binding}} = \Delta G_{\text{binding}}(\text{mutant}) - \Delta G_{\text{binding}}(\text{WT}) = \Delta G_m - \Delta G_s$ . Right panel: Bar plot indicating the calculated  $\Delta\Delta G_{\text{binding}}$  values for three mutants.

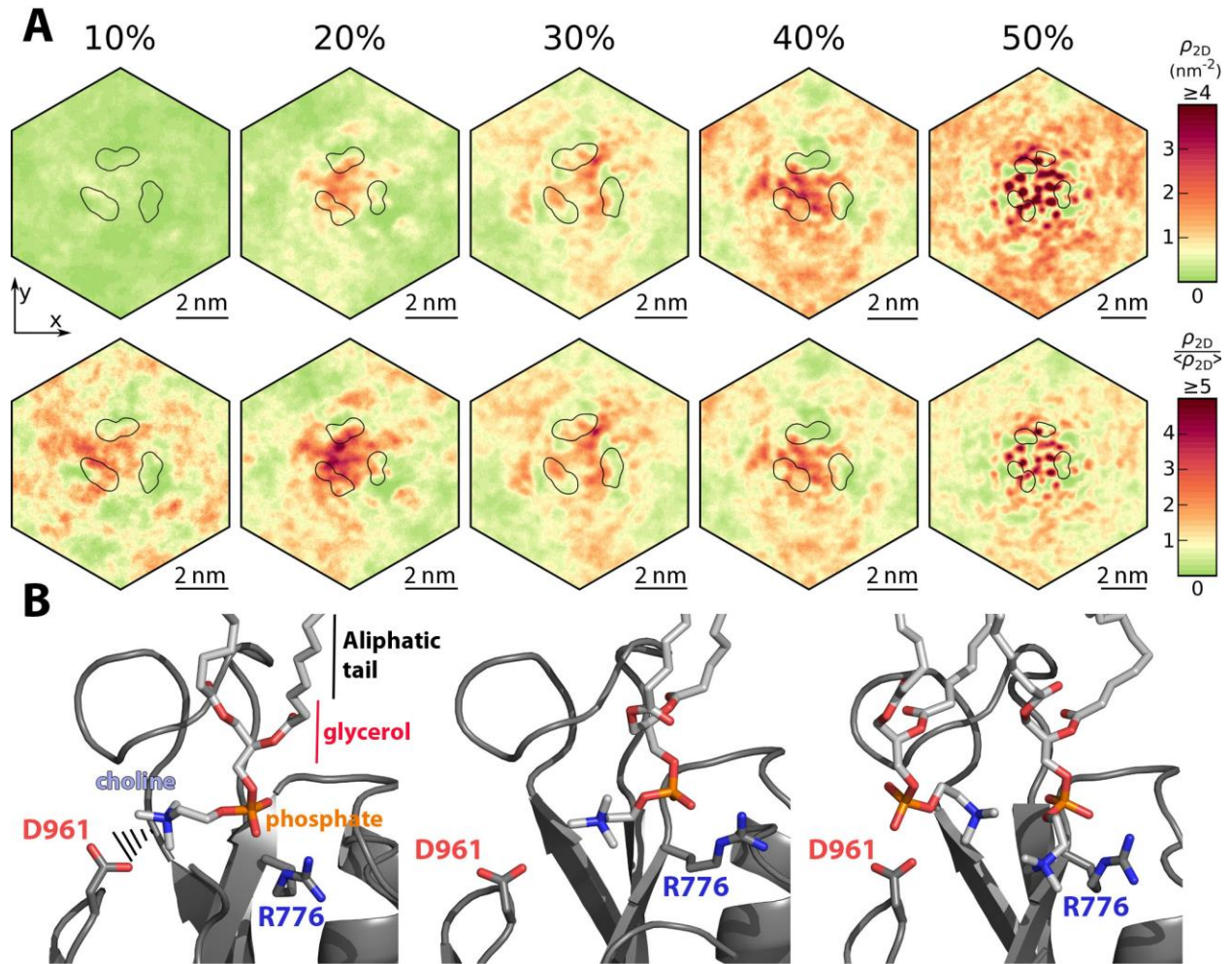


**Fig S7.** A) Absolute (top) and relative (bottom row) 2D density ( $\rho_{2D}$ ) of cholesterol in the leaflet in contact with the protein at various cholesterol ratios (labeled in %), plotted in the plane of the membrane using the average positions of cholesterol during the last 680 ns of the simulation (as outlined in Fig. S6). The average positions of the side chains of Trp821 and Phe826 are also shown as black outlines. B) Simulation snapshots in the region of the PC pocket from simulations in the 40% cholesterol system. The protein chain is shown as cartoon, Arg776, Asp961 side chains, and bound lipid molecules are shown as sticks. The carbon atoms are colored gray, and oxygen, nitrogen, and phosphorous atoms are blue, red, and orange, respectively. The interaction is very dynamic, in some snapshots, like the one on the right, there are two competing PC head groups at the entrance of the PC pocket of Gc.

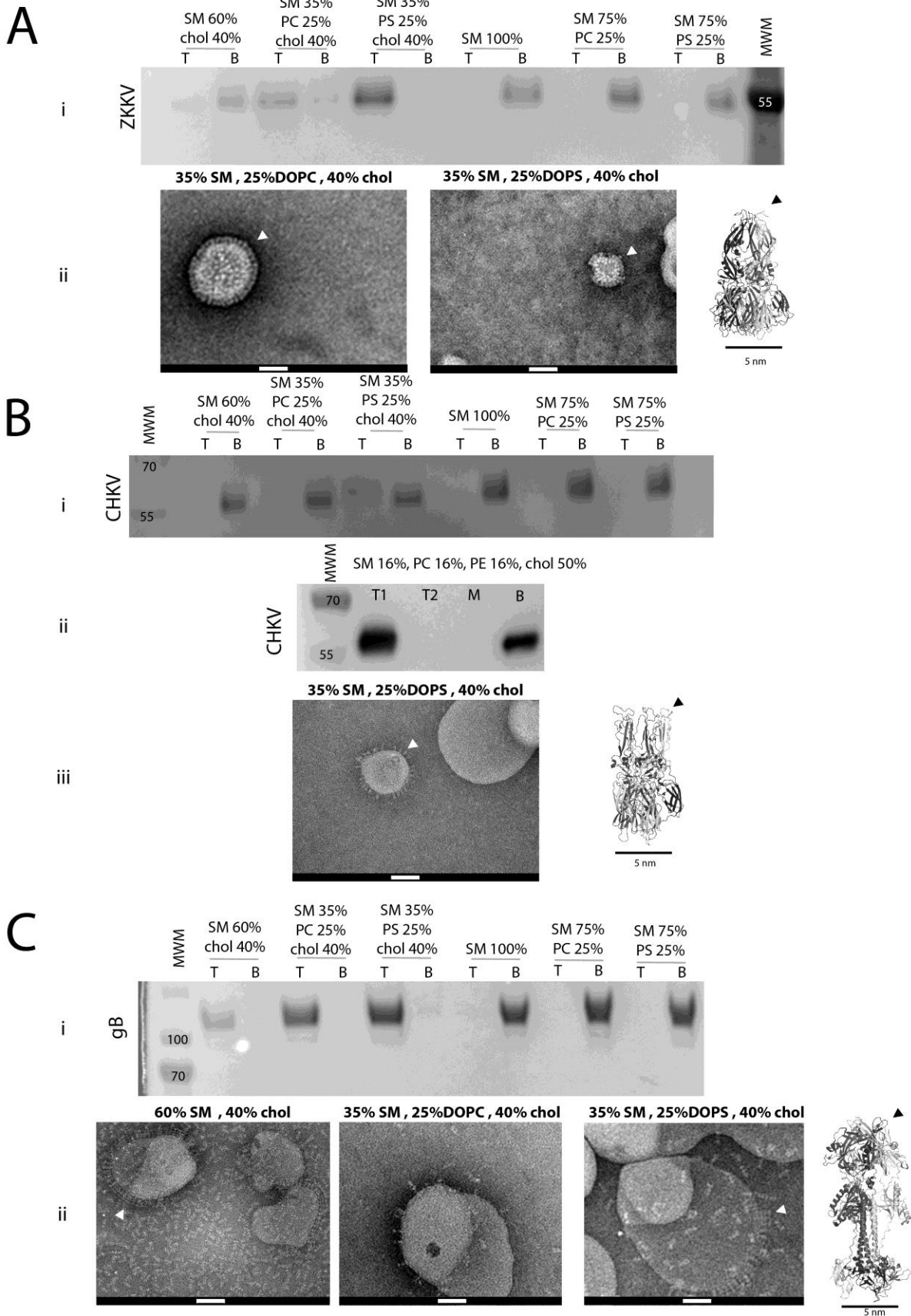


**Fig S8. The flavivirus and alphavirus class-II fusion proteins require GPL and cholesterol for membrane insertion.** In contrast to the RVFV Gc, which spontaneously convert into post-fusion trimers upon production in cell culture, the recombinant ectodomain of the flavivirus and alphavirus class-II fusion proteins are secreted in their pre-fusion form and trimerize only upon exposure to acid pH in the presence of liposomes, complicating the binding assessment by BLI or SPR. We therefore used ultracentrifugation in Optiprep gradients to test co-floitation of ZIKV E and CHIKV E1 ectodomains as described in the Methods Section, with liposomes of the composition indicated in the Figure. After ultracentrifugation, the top (labeled “T”) and bottom (“B”) fractions of the gradient were analyzed by SDS-PAGE and revealed by immunoblot using an antibody against the strep-tag (top panel in each case) and by visualizing the resulting proteoliposomes by negative stain EM (bottom panels in each case, A, B and C). The electron micrographs showed that the proteins associate in clusters at the liposome surface, as described earlier. A white arrowhead points to an inserted fusion protein ectodomain projecting from the liposomes. As a guide, a cartoon of the corresponding protein in the post-fusion form is displayed next to the micrographs. A black arrowhead points to the fusion loop, which is the side of the trimer that inserts into liposomes. A) the ZIKV E ectodomain: i) the protein was found to interact with the liposomes (i.e., was recovered from the top band) only when they contained GPLs (PS or PC), and not with SM+Cholesterol liposomes, or in the absence of cholesterol. ii) as a quality control, we have analyzed the liposomes positive for flotation by EM to confirm that ZIKV E ectodomain decorates their surface as other class-II fusion proteins. B). The CHIKV E1 ectodomain: i) it also showed no flotation in the absence of GPLs and cholesterol. Because the effect of the GPLs was less apparent in this case, we carried out a separate co-floitation experiment (ii) using a sucrose gradient and liposomes made of a different combination of GPLs (PC+PE instead of only one GPL). The gel shows that a substantial fraction of the CHIKV E1 ectodomain floated in this case. In ii, as a control, we also analyzed intermediate fractions of the gradient (T2 and M), not only the bottom (B) and top (T1) fraction (third row), which showed no protein, as expected. iii) EM negative staining showing that CHIKV E1 ectodomain decorates the surface of the liposomes as expected. C) the class-III fusion protein gB ectodomain used as control: i) it floats in presence of cholesterol independently of the presence of GPLs ii) as a quality control the ectodomain was imaged by EM in presence of liposomes containing cholesterol. As size references, we have included the structures of the flavivirus Dengue virus serotype 1 E ectodomain (4GSX), the SFV E1 ectodomain (1RER) and the Herpes Simplex type 1 virus gB (2GUM). Scale bars in the micrographs: 50 nm. The experiments show that in the presence of cholesterol, the class-III gB ectodomain control floated with the liposomes independently of the presence GPLs, but not the class-II fusion proteins (panels A–C, compare left lanes in the gels), which require GPLs.

## Supplementary Movies

**Movie S1.** Superposition of the Gc subunits in the various conformations. The Gc subunit in the monomer (pdb 4HJ1), dimer (pdb 4HJC) (both from (8)) and trimer (this work), are shown in ribbons colored according to the key on the side and superposed on domain II and most of domain I, showing that there is no difference in hinge angle between domains I and II as in other class-II fusion proteins, and that the conformational change is confined to a large rearrangement of domain III about the linker between domains I and III, and to the region of domain I from which the linker extends (i.e., the end of domain I that is opposite to the domain I–II interface). The invariable parts of the Gc subunit superpose with an rmsd of 0.9 Å over 326 atoms (monomer vs dimer), 1.55 Å over 283 atoms (trimer vs dimer) and 2.23 Å over 295 atoms (monomer vs trimer).

**Movie S2.** Morph of the transition from pre-fusion to post-fusion form. The two structures reported previously of the pre-fusion form (dimer, pdb 4HJ1; and monomer, pdb 4HJC) were used. As proposed by Dessau and Modis, the structure of the monomer appears as an extended intermediate, and it was not possible to morph directly from the dimer subunit (4HJ1) to that of the post-fusion trimer without introducing serious clashes. Instead, morphing first from the conformation of Gc in the dimer to that observed in the monomer (4HJC), allows to then transit to the final post-fusion form in the trimer without clashing.

**Movie S3.** Morph of the transition from pre-fusion to post-fusion form, as in Movie S2, showing that the side chains of Phe866 and Phe1018 make part of the hydrophobic core of domain I in the pre-fusion forms, and are dislodged from that location to become part of the inter-subunit interface within the post-fusion trimer. Phe1022, in the linker, also undergoes an important re-location.

**Movie S4.** Quality of the electron density map for C<sub>3</sub>PC binding pocket. Electron density maps colored at 1 $\sigma$  around the protein (blue map) and 0.9 $\sigma$  around the C<sub>3</sub>PC molecule (wheat map). The residues involved in binding are represented as sticks and labeled.

**Movie S5.** Molecular dynamics simulations of the interactions of Gc with membranes. Segments with duration of 150 ns from three different simulations are shown, with membranes containing only DOPC (left), DOPC plus 20% cholesterol (central) and 40% cholesterol (right). The polar heads of DOPC are represented as spheres and the aliphatic moiety as gray lines, the cholesterol is shown as red lines. The protein is shown in cartoon representation with the residues involved in the C<sub>3</sub>PC binding pocket as green spheres.

<b>Table S1. Data collection and refinement statistics</b>		
	<b>Gc-W821H</b>	<b>Gc-W821H / C<sub>3</sub>PC</b>
<b>Data collection</b>		
<b>Space group</b>	<i>P</i> 2 21 21	<i>P</i> 1 21 1
<b>Unit cell parameters</b>		
<b>a (Å)</b>	72.31	64.57
<b>b (Å)</b>	102.03	195.73
<b>c (Å)</b>	198.89	65.49
<b>α (°)</b>	90	90
<b>β (°)</b>	90	113.96
<b>γ (°)</b>	90	90
<b>% solvent</b>	50.7	52.2
<b>Resolution (Å)</b>	38.44-2.50	39.15-2.30
<b>Last resolution bin (Å)</b>	2.58-2.50	2.36-2.30
<b>Total observations<sup>a</sup></b>	180,550 (11,143)	279,562 (18,606)
<b>Unique reflections<sup>a</sup></b>	51,348 (4,374)	65,643 (4,612)
<b>Completeness (%)<sup>a</sup></b>	99.5 (99.1)	99.9 (99.9)
<b>Redundancy<sup>a</sup></b>	3.5 (2.5)	4.3 (4.0)
<b>&lt;I/σI&gt;<sup>a</sup></b>	10.0 (2.2)	9.3 (2.2)
<b>Rmerge (%)<sup>a</sup></b>	13.0 (73.5)	17.5 (68.9)
<b>Rpim (%)<sup>a</sup></b>	8.0 (54.1)	11.1 (42.9)
<b>CC(1/2)<sup>a</sup></b>	99.1 (66.5)	98.0 (61.7)
<b>Refinement</b>		
<b>PDB accession code</b>	6EGT	6EGU
<b>Resolution (Å)</b>	29.50-2.50	37.88-2.30
<b>Last resolution bin (Å)</b>	2.61-2.50	2.33-2.30
<b>No. reflections<sup>a</sup></b>	51,275 (6,159)	65,591 (2,578)
<b>No. test reflections<sup>a</sup></b>	2,036 (124)	3,306 (142)
<b>B refinement</b>	ISOTROPIC + TLS	ISOTROPIC + TLS
<b>Rfactor (%)<sup>a</sup></b>	19.5 (28.3)	18.3 (22.4)
<b>Rfree (%)<sup>a</sup></b>	23.5 (31.8)	23.2 (29.4)
<b>No. atoms<sup>b</sup></b>	3,439 / 3,420 / 3,413	3,420 / 3,406 / 3,409
<b>No. waters</b>	287	992
<b>No. MES atoms</b>	12 / 12	
<b>No. C<sub>3</sub>PC atoms<sup>b</sup></b>		24 / 19 / 24
<b>Mean B value (Å<sup>2</sup>)</b>		
<b>Protein + Glycans<sup>b</sup></b>	33.4 / 36.1 / 33.9	27.18 / 28.72 / 31.45
<b>Waters</b>	28.3	28.46
<b>MES<sup>c</sup></b>	48.4 / 84.5	
<b>C<sub>3</sub>PC<sup>b</sup></b>		51.6 / 86.3 / 40.6
<b>Root mean square deviations</b>		
<b>Bond lengths (Å)</b>	0.004	0.004
<b>Bond angles (°)</b>	0.920	0.757
<b>Ramachandran favored/outliers<sup>d</sup></b>	96.46/0.68	96.89/0.46

<sup>a</sup>Highest-resolution shell is shown in parenthesis<sup>b</sup>Number of atoms per chain (A/B/C)<sup>c</sup>Only two MES sites in the trimer were occupied.<sup>d</sup>Ramachandran statistics from Molprobit

<b>Table S2. Simulation data</b>						
<b>% Cholesterol present</b>	<b>0</b>	<b>10</b>	<b>20</b>	<b>30</b>	<b>40</b>	<b>50</b>
<b>Step 1 – Insertion into the membrane (pulling with harmonic potential)</b>						
<b>Force constant (kJ/(mol nm<sup>2</sup>))</b>	<b>1000</b>	<b>2000</b>				
<b>Pull velocity (nm/ns)</b>	<b>0.2</b>	<b>0.1</b>	<b>0.1</b>	<b>0.2</b>	<b>0.2</b>	<b>0.2</b>
<b>Pulling time (ns)</b>	<b>27.5</b>	<b>35</b>	<b>35</b>	<b>22</b>	<b>23</b>	<b>17</b>
<b>Translation of membrane COM<sup>¶</sup> (nm)</b>	<b>1.32</b>	<b>1.55</b>	<b>1.53</b>	<b>1.52</b>	<b>1.46</b>	<b>0.85</b>
<b>Step 2 – Membrane equilibration (protein-membrane distance restraint with harmonic potential)</b>						
<b>Temperature (K)</b>	<b>373</b>					<b>403</b>
<b>Force constant (kJ/(mol nm<sup>2</sup>))</b>	<b>4000</b>					
<b>Time (ns)</b>	<b>71</b>	<b>200</b>	<b>200</b>	<b>72</b>	<b>200</b>	<b>75</b>
<b>Step 3 – Equilibration of COM (distance restraint released)</b>						
<b>Time (ns)</b>	<b>5</b>					
<b>Temperature (K)</b>	<b>310</b>					
<b>Step 4 – Production simulations (position restraints on protein heavy atoms released)</b>						
<b>Temperature (K)</b>	<b>310</b>					
<b>Number of independent production runs</b>	<b>3</b>	<b>3</b>	<b>3</b>	<b>4</b>	<b>3</b>	<b>3</b>
<b>Simulation 1 – Time (ns) (last 200ns used for analysis)</b>	<b>450</b>	<b>550</b>	<b>550</b>	<b>550</b>	<b>550</b>	<b>600</b>
<b>Simulation 2 – Time (ns) (last 480ns used for analysis)</b>	<b>500</b>					

<sup>¶</sup>The translation is with respect to the membrane COM at time 0 of the respective pulling simulation (before Step 1 in the diagram of Fig. S7).

<b>Table S3. Free energy calculations. All values are in kJ mol<sup>-1</sup>.</b>			
<b>Transformation</b>	<b><math>\Delta G_m</math></b>	<b><math>\Delta G_s</math></b>	<b><math>\Delta\Delta G_{binding}</math></b>
<b>W821H<sup>a</sup></b>	<b>-257.9±1.6</b>	<b>-303.8±0.4</b>	<b>45.9±1.6</b>
<b>W821A<sup>a</sup></b>	<b>-47.6±1.5</b>	<b>-86.4±0.3</b>	<b>38.8±1.5</b>
<b>F826A<sup>b</sup></b>	<b>-31.0±1.1</b>	<b>-53.4±0.2</b>	<b>22.4±1.1</b>

Transformation performed in the wild type protein<sup>a</sup> or in the W821A mutant<sup>b</sup>.

## References and Notes

1. R. Daubney, J. R. Hudson, P. C. Garnham, Enzootic hepatitis or rift valley fever. An undescribed virus disease of sheep cattle and man from East Africa. *J. Pathol.* **34**, 545–579 (1931). [doi:10.1002/path.1700340418](https://doi.org/10.1002/path.1700340418)
2. R. Swanepoel, J. A. W. Coetzer, in *Infectious Diseases of Livestock*, J. Coetzer, R. Tustin, Eds. (Oxford Univ. Press, 2004), vol. 1, chap. 95, pp. 1037–1070.
3. K. J. Linthicum, S. C. Britch, A. Anyamba, Rift Valley fever: An emerging mosquito-borne disease. *Annu. Rev. Entomol.* **61**, 395–415 (2016). [doi:10.1146/annurev-ento-010715-023819](https://doi.org/10.1146/annurev-ento-010715-023819) [Medline](#)
4. H. H. Balkhy, Z. A. Memish, Rift Valley fever: An uninvited zoonosis in the Arabian peninsula. *Int. J. Antimicrob. Agents* **21**, 153–157 (2003). [doi:10.1016/S0924-8579\(02\)00295-9](https://doi.org/10.1016/S0924-8579(02)00295-9) [Medline](#)
5. V. Chevalier, M. Pépin, L. Plée, R. Lancelot, Rift Valley fever—A threat for Europe? *Euro Surveill.* **15**, 19506 (2010). [Medline](#)
6. A. N. Freiberg, M. B. Sherman, M. C. Morais, M. R. Holbrook, S. J. Watowich, Three-dimensional organization of Rift Valley fever virus revealed by cryoelectron tomography. *J. Virol.* **82**, 10341–10348 (2008). [doi:10.1128/JVI.01191-08](https://doi.org/10.1128/JVI.01191-08) [Medline](#)
7. J. T. Huiskonen, A. K. Overby, F. Weber, K. Grünewald, Electron cryo-microscopy and single-particle averaging of Rift Valley fever virus: Evidence for GN-GC glycoprotein heterodimers. *J. Virol.* **83**, 3762–3769 (2009). [doi:10.1128/JVI.02483-08](https://doi.org/10.1128/JVI.02483-08) [Medline](#)
8. M. B. Sherman, A. N. Freiberg, M. R. Holbrook, S. J. Watowich, Single-particle cryo-electron microscopy of Rift Valley fever virus. *Virology* **387**, 11–15 (2009). [doi:10.1016/j.virol.2009.02.038](https://doi.org/10.1016/j.virol.2009.02.038) [Medline](#)
9. P. Y. Lozach, A. Kühbacher, R. Meier, R. Mancini, D. Bitto, M. Bouloy, A. Helenius, DC-SIGN as a receptor for phleboviruses. *Cell Host Microbe* **10**, 75–88 (2011). [doi:10.1016/j.chom.2011.06.007](https://doi.org/10.1016/j.chom.2011.06.007) [Medline](#)
10. M. Dessau, Y. Modis, Crystal structure of glycoprotein C from Rift Valley fever virus. *Proc. Natl. Acad. Sci. U.S.A.* **110**, 1696–1701 (2013). [doi:10.1073/pnas.1217780110](https://doi.org/10.1073/pnas.1217780110) [Medline](#)
11. F. A. Rey, F. X. Heinz, C. Mandl, C. Kunz, S. C. Harrison, The envelope glycoprotein from tick-borne encephalitis virus at 2 Å resolution. *Nature* **375**, 291–298 (1995). [doi:10.1038/375291a0](https://doi.org/10.1038/375291a0) [Medline](#)
12. J. Lescar, A. Roussel, M. W. Wien, J. Navaza, S. D. Fuller, G. Wengler, G. Wengler, F. A. Rey, The fusion glycoprotein shell of Semliki Forest virus: An icosahedral assembly primed for fusogenic activation at endosomal pH. *Cell* **105**, 137–148 (2001). [doi:10.1016/S0092-8674\(01\)00303-8](https://doi.org/10.1016/S0092-8674(01)00303-8) [Medline](#)
13. S. Igonet, F. A. Rey, SnapShot: Viral and eukaryotic protein fusogens. *Cell* **151**, 1634–1634.e1 (2012). [doi:10.1016/j.cell.2012.11.041](https://doi.org/10.1016/j.cell.2012.11.041) [Medline](#)
14. S. C. Harrison, Viral membrane fusion. *Virology* **479-480**, 498–507 (2015). [doi:10.1016/j.virol.2015.03.043](https://doi.org/10.1016/j.virol.2015.03.043) [Medline](#)

15. J. L. Lorieau, J. M. Louis, A. Bax, The complete influenza hemagglutinin fusion domain adopts a tight helical hairpin arrangement at the lipid:water interface. *Proc. Natl. Acad. Sci. U.S.A.* **107**, 11341–11346 (2010). [doi:10.1073/pnas.1006142107](https://doi.org/10.1073/pnas.1006142107) [Medline](#)
16. W. Qiang, M. L. Bodner, D. P. Weliky, Solid-state NMR spectroscopy of human immunodeficiency virus fusion peptides associated with host-cell-like membranes: 2D correlation spectra and distance measurements support a fully extended conformation and models for specific antiparallel strand registries. *J. Am. Chem. Soc.* **130**, 5459–5471 (2008). [doi:10.1021/ja077302m](https://doi.org/10.1021/ja077302m) [Medline](#)
17. B. Apellániz, N. Huarte, E. Largo, J. L. Nieva, The three lives of viral fusion peptides. *Chem. Phys. Lipids* **181**, 40–55 (2014). [doi:10.1016/j.chemphyslip.2014.03.003](https://doi.org/10.1016/j.chemphyslip.2014.03.003) [Medline](#)
18. S. Bressanelli, K. Stiasny, S. L. Allison, E. A. Stura, S. Duquerroy, J. Lescar, F. X. Heinz, F. A. Rey, Structure of a flavivirus envelope glycoprotein in its low-pH-induced membrane fusion conformation. *EMBO J.* **23**, 728–738 (2004). [doi:10.1038/sj.emboj.7600064](https://doi.org/10.1038/sj.emboj.7600064) [Medline](#)
19. D. L. Gibbons, M.-C. Vaney, A. Roussel, A. Vigouroux, B. Reilly, J. Lepault, M. Kielian, F. A. Rey, Conformational change and protein-protein interactions of the fusion protein of Semliki Forest virus. *Nature* **427**, 320–325 (2004). [doi:10.1038/nature02239](https://doi.org/10.1038/nature02239) [Medline](#)
20. S. Halldorsson, A.-J. Behrens, K. Harlos, J. T. Huisken, R. M. Elliott, M. Crispin, B. Brennan, T. A. Bowden, Structure of a phleboviral envelope glycoprotein reveals a consolidated model of membrane fusion. *Proc. Natl. Acad. Sci. U.S.A.* **113**, 7154–7159 (2016). [doi:10.1073/pnas.1603827113](https://doi.org/10.1073/pnas.1603827113) [Medline](#)
21. Y. Modis, S. Ogata, D. Clements, S. C. Harrison, Structure of the dengue virus envelope protein after membrane fusion. *Nature* **427**, 313–319 (2004). [doi:10.1038/nature02165](https://doi.org/10.1038/nature02165) [Medline](#)
22. S. Roche, F. A. Rey, Y. Gaudin, S. Bressanelli, Structure of the prefusion form of the vesicular stomatitis virus glycoprotein G. *Science* **315**, 843–848 (2007). [doi:10.1126/science.1135710](https://doi.org/10.1126/science.1135710) [Medline](#)
23. D. Bitto, S. Halldorsson, A. Caputo, J. T. Huisken, Low pH and anionic lipid-dependent fusion of Uukuniemi phlebovirus to liposomes. *J. Biol. Chem.* **291**, 6412–6422 (2016). [doi:10.1074/jbc.M115.691113](https://doi.org/10.1074/jbc.M115.691113) [Medline](#)
24. M. Kielian, C. Chanel-Vos, M. Liao, Alphavirus entry and membrane fusion. *Viruses* **2**, 796–825 (2010). [doi:10.3390/v2040796](https://doi.org/10.3390/v2040796) [Medline](#)
25. A. Wilder-Smith, D. J. Gubler, S. C. Weaver, T. P. Monath, D. L. Heymann, T. W. Scott, Epidemic arboviral diseases: Priorities for research and public health. *Lancet Infect. Dis.* **17**, e101–e106 (2017). [Medline](#)
26. M. Umashankar, C. Sánchez-San Martín, M. Liao, B. Reilly, A. Guo, G. Taylor, M. Kielian, Differential cholesterol binding by class II fusion proteins determines membrane fusion properties. *J. Virol.* **82**, 9245–9253 (2008). [doi:10.1128/JVI.00975-08](https://doi.org/10.1128/JVI.00975-08) [Medline](#)
27. K. A. Tssetsarkin, D. L. Vanlandingham, C. E. McGee, S. Higgs, A single mutation in chikungunya virus affects vector specificity and epidemic potential. *PLOS Pathog.* **3**, e201 (2007). [doi:10.1371/journal.ppat.0030201](https://doi.org/10.1371/journal.ppat.0030201) [Medline](#)

28. I. Schuffenecker, I. Itean, A. Michault, S. Murri, L. Frangeul, M.-C. Vaney, R. Lavenir, N. Pardigon, J.-M. Reynes, F. Pettinelli, L. Biscornet, L. Diancourt, S. Michel, S. Duquerroy, G. Guigon, M.-P. Frenkiel, A.-C. Bréhin, N. Cubito, P. Desprès, F. Kunst, F. A. Rey, H. Zeller, S. Brisse, Genome microevolution of chikungunya viruses causing the Indian Ocean outbreak. *PLOS Med.* **3**, e263 (2006). [doi:10.1371/journal.pmed.0030263](https://doi.org/10.1371/journal.pmed.0030263) [Medline](#)
29. Materials and methods are available as supplementary materials.
30. J. Pérez-Vargas, T. Krey, C. Valansi, O. Avinoam, A. Haouz, M. Jamin, H. Raveh-Barak, B. Podbilewicz, F. A. Rey, Structural basis of eukaryotic cell-cell fusion. *Cell* **157**, 407–419 (2014). [doi:10.1016/j.cell.2014.02.020](https://doi.org/10.1016/j.cell.2014.02.020) [Medline](#)
31. S. Murakami, K. Terasaki, S. I. Ramirez, J. C. Morrill, S. Makino, Development of a novel, single-cycle replicable rift valley Fever vaccine. *PLOS Negl. Trop. Dis.* **8**, e2746 (2014). [doi:10.1371/journal.pntd.0002746](https://doi.org/10.1371/journal.pntd.0002746) [Medline](#)
32. J. E. Voss, M.-C. Vaney, S. Duquerroy, C. Vonnrhein, C. Girard-Blanc, E. Crublet, A. Thompson, G. Bricogne, F. A. Rey, Glycoprotein organization of chikungunya virus particles revealed by x-ray crystallography. *Nature* **468**, 709–712 (2010). [doi:10.1038/nature09555](https://doi.org/10.1038/nature09555) [Medline](#)
33. D. L. Gibbons, I. Erk, B. Reilly, J. Navaza, M. Kielian, F. A. Rey, J. Lepault, Visualization of the target-membrane-inserted fusion protein of Semliki Forest virus by combined electron microscopy and crystallography. *Cell* **114**, 573–583 (2003). [doi:10.1016/S0092-8674\(03\)00683-4](https://doi.org/10.1016/S0092-8674(03)00683-4) [Medline](#)
34. X. Han, L. K. Tamm, A host-guest system to study structure-function relationships of membrane fusion peptides. *Proc. Natl. Acad. Sci. U.S.A.* **97**, 13097–13102 (2000). [doi:10.1073/pnas.230212097](https://doi.org/10.1073/pnas.230212097) [Medline](#)
35. E. Zaitseva, S. T. Yang, K. Melikov, S. Pourmal, L. V. Chernomordik, Dengue virus ensures its fusion in late endosomes using compartment-specific lipids. *PLOS Pathog.* **6**, e1001131 (2010). [doi:10.1371/journal.ppat.1001131](https://doi.org/10.1371/journal.ppat.1001131) [Medline](#)
36. S. Q. Fan, W. Huang, L. X. Wang, Remarkable transglycosylation activity of glycosynthase mutants of endo-D, an endo- $\beta$ -N-acetylglucosaminidase from *Streptococcus pneumoniae*. *J. Biol. Chem.* **287**, 11272–11281 (2012). [doi:10.1074/jbc.M112.340497](https://doi.org/10.1074/jbc.M112.340497) [Medline](#)
37. W. Kabsch, XDS. *Acta Crystallogr. D* **66**, 125–132 (2010). [doi:10.1107/S0907444909047337](https://doi.org/10.1107/S0907444909047337) [Medline](#)
38. P. R. Evans, G. N. Murshudov, How good are my data and what is the resolution? *Acta Crystallogr. D* **69**, 1204–1214 (2013). [doi:10.1107/S0907444913000061](https://doi.org/10.1107/S0907444913000061) [Medline](#)
39. A. J. McCoy, R. W. Grosse-Kunstleve, P. D. Adams, M. D. Winn, L. C. Storoni, R. J. Read, Phaser crystallographic software. *J. Appl. Crystallogr.* **40**, 658–674 (2007). [doi:10.1107/S0021889807021206](https://doi.org/10.1107/S0021889807021206) [Medline](#)
40. P. Emsley, B. Lohkamp, W. G. Scott, K. Cowtan, Features and development of Coot. *Acta Crystallogr. D* **66**, 486–501 (2010). [doi:10.1107/S0907444910007493](https://doi.org/10.1107/S0907444910007493) [Medline](#)
41. P. D. Adams, P. V. Afonine, G. Bunkóczi, V. B. Chen, I. W. Davis, N. Echols, J. J. Headd, L.-W. Hung, G. J. Kapral, R. W. Grosse-Kunstleve, A. J. McCoy, N. W. Moriarty, R.

- Oeffner, R. J. Read, D. C. Richardson, J. S. Richardson, T. C. Terwilliger, P. H. Zwart, *PHENIX: A comprehensive Python-based system for macromolecular structure solution. Acta Crystallogr. D* **66**, 213–221 (2010). [doi:10.1107/S0907444909052925](https://doi.org/10.1107/S0907444909052925) [Medline](#)
42. M. J. Abraham, T. Murtola, R. Schulz, S. Páll, J. C. Smith, B. Hess, E. Lindahl, GROMACS: High performance molecular simulations through multi-level parallelism from laptops to supercomputers. *SoftwareX* **1-2**, 19–25 (2015). [doi:10.1016/j.softx.2015.06.001](https://doi.org/10.1016/j.softx.2015.06.001)
43. W. L. Jorgensen, J. Chandrasekhar, J. D. Madura, R. W. Impey, M. L. Klein, Comparison of simple potential functions for simulating liquid water. *J. Chem. Phys.* **79**, 926–935 (1983). [doi:10.1063/1.445869](https://doi.org/10.1063/1.445869)
44. J. P. M. Jämbeck, A. P. Lyubartsev, Another piece of the membrane puzzle: Extending slipids further. *J. Chem. Theory Comput.* **9**, 774–784 (2013). [doi:10.1021/ct300777p](https://doi.org/10.1021/ct300777p) [Medline](#)
45. K. Lindorff-Larsen, S. Piana, K. Palmo, P. Maragakis, J. L. Klepeis, R. O. Dror, D. E. Shaw, Improved side-chain torsion potentials for the Amber ff99SB protein force field. *Proteins* **78**, 1950–1958 (2010). [Medline](#)
46. R. B. Best, G. Hummer, Optimized molecular dynamics force fields applied to the helix-coil transition of polypeptides. *J. Phys. Chem. B* **113**, 9004–9015 (2009). [doi:10.1021/jp901540t](https://doi.org/10.1021/jp901540t) [Medline](#)
47. G. Bussi, D. Donadio, M. Parrinello, Canonical sampling through velocity rescaling. *J. Chem. Phys.* **126**, 014101 (2007). [doi:10.1063/1.2408420](https://doi.org/10.1063/1.2408420) [Medline](#)
48. H. J. C. Berendsen, J. P. M. Postma, W. F. van Gunsteren, A. DiNola, J. R. Haak, Molecular dynamics with coupling to an external bath. *J. Chem. Phys.* **81**, 3684–3690 (1984). [doi:10.1063/1.448118](https://doi.org/10.1063/1.448118)
49. M. Parrinello, A. Rahman, Polymorphic transitions in single crystals: A new molecular dynamics method. *J. Appl. Phys.* **52**, 7182–7190 (1981). [doi:10.1063/1.328693](https://doi.org/10.1063/1.328693)
50. U. Essmann, L. Perera, M. L. Berkowitz, T. Darden, H. Lee, L. G. Pedersen, A smooth particle mesh Ewald method. *J. Chem. Phys.* **103**, 8577–8593 (1995). [doi:10.1063/1.470117](https://doi.org/10.1063/1.470117)
51. T. Darden, D. York, L. Pedersen, Particle mesh Ewald: An  $N \cdot \log(N)$  method for Ewald sums in large systems. *J. Chem. Phys.* **98**, 10089–10092 (1993). [doi:10.1063/1.464397](https://doi.org/10.1063/1.464397)
52. B. Hess, P-LINCS: A parallel linear constraint solver for molecular simulation. *J. Chem. Theory Comput.* **4**, 116–122 (2008). [doi:10.1021/ct700200b](https://doi.org/10.1021/ct700200b) [Medline](#)
53. S. Miyamoto, P. A. Kollman, SETTLE: An analytical version of the SHAKE and RATTLE algorithms for rigid water models. *J. Comput. Chem.* **13**, 952–962 (1992). [doi:10.1002/jcc.540130805](https://doi.org/10.1002/jcc.540130805)
54. W. L. De Lano, The PyMOL Molecular Graphics System, version 1.8.2 (Schrödinger, LLC, 2002).
55. B. Hess, Convergence of sampling in protein simulations. *Phys. Rev. E* **65**, 031910 (2002). [doi:10.1103/PhysRevE.65.031910](https://doi.org/10.1103/PhysRevE.65.031910) [Medline](#)